REPORT DOCUMENTATION PAGE

Form Approved
OMB No. 0704-0188

1. AGENCY USE ONLY (*Leave Blank*)	2. REPORT DATE	3. REPORT TYPE AND DATES COVERED
	April 1997	Final Report, 1 Oct 1994 - 28 Feb 1997

4. TITLE AND SUBTITLE
Seismic Sources and Structure in Iran and the Caucasus from Joint Seismic Program Array Data

5. FUNDING NUMBERS
AFOSR F49620-95-1-0002

6. AUTHORS
Geoffrey A. Abers

AFOSR-TR-97
0194

7. PERFORMING ORGANIZATION NAME(S) AND ADDRESS(ES)
University of Kansas
Geology Department, 120 Lindley Hall
Lawrence, KS 66045

9. SPONSORING / MONITORING AGENCY NAME(S) AND ADDRESS(ES)
Air Force Office of Scientific Research
AFOSR/NM
110 Duncan Avenue Suite B115
Bolling AFB DC 20332-6448

10. SPONSORING / MONITORING AGENCY REPORT NUMBER

11. SUPPLEMENTARY NOTES

12a. DISTRIBUTION / AVAILABILITY STATEMENT
unlimited

DISTRIBUTION STATEMENT A
Approved for public release
Distribution Unlimited

12b. DISTRIBUTION CODE

13. ABSTRACT (*Maximum 200 words*)

Recently-deployed seismic networks and arrays along the southern Former Soviet Union are characterized, including aspects of wave propagation that affect their ability to detect signals from the Iranian Plateau and surrounding regions. Signals at the Caucasus Network (CNET, deployed 1992-1994) were strongly affected by attenuation along paths that transect the Caucasus or Iranian Plateau, unlike signals to the north. At long paths (5-25°) the Caucasus and Iranian Plateau, little or no *S* wave energy was observed at frequencies above 0.5 Hz, and no discernable *Lg*. At distances > 10° few events events smaller than $m_b < 4.5$ were detectable. At shorter distances, analysis of body wave spectra were used to accurately quantify the attenuation boundary between the Greater Caucasus and Russian Platform. This transition serves as a proxy for that along most of the southern margins of Russia. Analysis of several hundred signals at distances <4° showed a factor-of-3 decrease in attenuation from mountains to shield. These observations, at 1-15 Hz, suggest that signal amplitude at frequencies used for magnitude calibration will vary considerably from shield to mountains. The nature of this transition and its possible causes are discussed.

14. SUBJECT TERMS	15. NUMBER OF PAGES
Seismic Waves, Caucasus, Middle East, Attenuation, Nuclear Monitoring	
	16. PRICE CODE

17. SECURITY CLASSIFICATION OF REPORT	18. SECURITY CLASSIFICATION OF THIS PAGE	19. SECURITY CLASSIFICATION OF ABSTRACT	20. LIMITATION OF ABSTRACT
UNCLASSIFIED			

NSN 7540-01-280-5500

Standard Form 298 (Rev. 2-89)
Prescribed by ANSI Std. Z39-1
298-102

19970604 152

DTIC QUALITY INSPECTED 2

Seismic sources and structure in Iran and the Caucasus from Joint Seismic Program array data

Final Technical Report

AFOSR Grant F49620-95-1-0002

PI: Geoffrey A. Abers
Geology Department, University of Kansas, Lawrence KS

Table of Contents

OBJECTIVE

We evaluate and characterize seismic data from digital network and array sites in and around the Former Soviet Union, in order to provide new constraints on seismic wave propagation characteristics in the Caucasus Ranges, Middle East and Iranian Plateau. Strong changes in the attenuation and velocity behavior of seismic waves are associated with the mountain belts here, and make it difficult to infer wave behavior from experiences gained within stable cratons. Seismograms from the JSP-Caucasus Seismic Network collected since 1991 include a large number of local and regional events in the region. These waveforms are used for assessing the amplitude and phase of major wave groups along regional paths, and constraining earth structure beneath the network. Results provide information on the behavior of common event discriminants and detection thresholds for regional paths.

RESEARCH ACCOMPLISHED

Severe changes in wave behavior are observed between paths that cross the Caucasus and other Alpine-Himalayan mountain belts, and those that do not (Figure 1). These changes represent substantial attenuation of phases often used to discriminate explosions from earthquakes and to estimate event size and type, such as *Lg* and other high-frequency surface-related phases. Work to date has concentrated on quantifying the behavior of seismic waves as they cross the Caucasus, mostly by examining phase amplitudes for events within 10° of the Caucasus Seismic Network (CNet). Other facilities, such as the Geyokcha, Turkmenistan array also provide digital seismograms that can give complementary information.

I. Body wave attenuation across the Greater Caucasus range front

Summary. A regionally abrupt boundary in seismic attenuation is documented between the Russian platform and the tectonically active Greater Caucasus. Attenuation (Q^{-1}) is measured from body waves recorded by a digital seismic network that straddled north flank of the Greater Caucasus from 1992 to 1994. Spectral fall-off of body waves is measured from 186 events within 4° distance of the stations, and a frequency-independent attenuation parameter (t^*) and source corner frequency is determined from fits to amplitude spectra. Most fits are at frequencies between 2 and 15 Hz, limited by background noise. These t^* measurements are then inverted for Q^{-1}, for parameterizations of varying complexity. Results show Q_S of 775 ±75 and 2060 ±315 for mountain and platform paths, respectively, and $Q_P \sim Q_S$. Inversions show more than 30% variance reduction for parameterizations that allow Q^{-1} to vary laterally relative to laterally homogeneous parameterizations. Site corrections also significantly reduce variance of fit between predicted and measured t^*. High attenuation is observed beneath high topography, separated by a sharp boundary from the low-Q^{-1} platform. Comparison of body wave spectra to those of coda suggests intrinsic absorption rather than scattering controls the Q^{-1} measurements, at least beneath the mountains. If the observed Q^{-1} contrasts are due to changes in temperature, they suggest 70-400° C higher temperatures beneath the mountain relative to the platform. These temperature increases may not be high enough to generate widespread partial melting beneath the mountains, but are sufficient to produce regional metamorphism, and can contribute substantially to isostatic compensation of the mountains. Whatever the cause, these data show that the boundary in seismic attenuation is abrupt and

large between stable shield and an adjacent mountain belt, showing that Q^{-1} is a sensitive indicator of tectonic process.

I.1 Introduction

Eurasia is dominated by a first-order distinction between stable shields and active mountain belts associated with Alpine-Himalayan collision. The tectonic style of these mountain belts vary considerably (e.g. Jackson & McKenzie 1984), but in many cases the boundary between stable Eurasian cratonic regions and the mountains to their south are abrupt. For example, peaks of the Greater Caucasus exceed 5 km in elevation, within view of the Russian (Scythian) platform where elevations are uniformly below 500 m (Figure 1). At long wavelengths (≥1000 km), it has long been known that differences between the deeper structures of shields and mountains are also large. Seismic wave propagation over regional distances beneath stable Eurasia is very efficient (Zhang & Lay 1994; Mitchell, Xie & Pan 1996; Kim 1987), while many seismic waves transmit poorly through adjacent mountains (Kadinsky-Cade et al. 1981; Rodgers, Hearn & Ni 1997).

It is less clear how these first-order transitions in wave propagation manifest themselves over scales of tens of km, scales at which many tectonic processes operate. Transitions at depth may correspond to geologic boundaries on the surface, to topographic boundaries, or neither. For example, across the Rocky Mountain front of North America, it has been found that subsurface boundaries are offset by hundreds of kilometers from the topographic range front (e.g. Lee & Grand 1996; Humphreys & Dueker 1994). Here, we take advantage of new seismic data across one such boundary, that between the Greater Caucasus and Russian platform to explore the subsurface. Because the effect of attenuation is strong (Figure 2) and well sampled, we use attenuation variations to describe the shield-mountain transition. A second goal of this study is to better understand lateral variations of signal propagation characteristics, which play a key role in seismic monitoring at regional distances. We find that large-scale boundaries between tectonic provinces can generate sharp boundaries to seismic attenuation, and that the boundary in the Caucasus at least correlates well with that seen in topography.

The method used here to determine Q is based on measurements of the spectral fall-off of body waves, similar to Hough et al. (1988a). This approach gets around many of the problems associated with Q determinations based on absolute amplitudes, which can be greatly affected by near-surface effects, focusing and defocusing, and source behavior (e.g. Frankel & Wennerberg 1987). Body waves also sample energy that travels close to the ray-theoretical phase arrival time, so that the sampling volume is small, unlike the large volumes sampled by coda waves. Hence resolution of structures is much greater than for coda techniques, and we can resolve a sharp attenuation boundary within the crust that coincides with the boundary between tectonically active and inactive regions. The sharpness of this boundary suggests that long-wavelength Q measures may be severely aliases across mountain fronts. As well, the mechanisms for producing low Q may be closely tied to the mechanisms for producing topography in collisional belts.

I.2 Regional Setting and Seismicity

The Greater Caucasus accommodate Cenozoic convergence between Eurasia and Arabia, currently 29 mm/yr at N26°W in this region (DeMets et al. 1990). The mountains strike SE-NW between the Black and Caspian seas, and form a part of the continuous orogenic belt along the southern edge of the Russian Platform. The southern edge of the

Platform is covered with Mesozoic and Cenozoic sediments, overlying Hercynian basement of the Scythian craton (Adamiya et al. 1992). Uplift and convergence began in the Middle-to-Late Miocene, and intensified during Mid-Pliocene (Burtman 1989). The core of the Greater Caucasus consists of Precambrian and Paleozoic igneous and metamorphic rocks (e.g. Zonenshain, Kuzmin & Natapov 1990), while the southern slope of the mountains is a thrust belt involving backarc-type sediments, deposited throughout the Jurassic, Cretaceous and Paleogene (Zonenshain & Le Pichon 1986). North-dipping thrust sheets or nappes characterize extensive deformation on the southern slope of the Greater Caucasus, while a gently north-dipping monocline bounds the northern slope (e.g. Philip et al. 1989). Late Quaternary volcanism occurs in isolated locations throughout western part of the Greater Caucasus (Philip et al. 1989), including Mt. Elbruz at the SE edge of the network (Figure 1), which may be still active (Kovalev & Masurenko 1972).

The region is seismically active, with the majority of seismicity concentrated to the south of the Greater Caucasus near the Iranian plateau (e.g. Jackson & McKenzie 1984). The April 29, 1991 Racha earthquake (moment magnitude M_W=7.3) is the largest instrumentally recorded earthquake in the Greater Caucasus (Triep et al. 1995; Gorshkov 1984). The focal mechanisms of that and smaller earthquakes show thrust faults striking parallel to the mountains, with shallow-dipping planes dipping to the north (Jackson & McKenzie 1984). Thus, the north-dipping thrust faults that bound the southern slopes of the Greater Caucasus are still active (Triep et al. 1995). Many of the events studied here are near the 1991 aftershock zone (near 43°E, 42°N). East of 45°E most earthquakes studied here occur north of the mountains, where a south-dipping thrust belt is exposed (Figure 1).

The Caucasus are a region of anomalously low seismic velocities and high attenuation (low Q). Rautian, Khalturin & Shengeliya (1979) show coda Q values near 330 at 1 Hz. Kadinsky-Cade et al. (1981) and Rodgers et al. (1997) both show that at regional distances (5-25°) the phase S_n propagates weakly or not at all at frequencies near 1 Hz, through the Caucasus. As well, L_g is shown in these studies to propagate poorly across the Black Sea, the southern Caspian Sea, and through some regions of high topography. The strong S_n attenuation led these authors to postulate the existence of widespread partial melt beneath the Caucasus within the uppermost mantle. A similar inference was made by Hearn & Ni (1994) who observed extremely low P_n velocities, near 7.6 km/s, associated with the Caucasus. Our results confirm and quantify the low attenuation values associated with the Caucasus, and document the northern boundary of the attenuative region. We show, however, that the data are consistent with elevated temperatures and do not require that partial melt be present.

I.3 Data and Methodology

Data were recorded by the Greater Caucasus seismic network, operated from 1991 to 1994 through a cooperative project among IRIS, Lamont-Doherty Earth Observatory and the OME-Obninsk group (Abers 1994). Stations were located on the northern slope of the Greater Caucasus, and straddled the transition from the Greater Caucasus to the Russian Platform (Figure 1). The northern stations (NAG, MIC, KUB) lie on a flat-lying, poorly consolidated Neogene sediments, while southern stations (KIV, GUM, KNG) lie on a tilted, well-lithified Mesozoic sandstones and limestones. The network consisted of up to six digitally telemetered three-component intermediate-period sensors (Kinemetrics SV/SH-1), digitized at 60 samples/s (sps) by Nanometrics RD-3 digitizers. The configuration has a flat response to velocity at frequencies between 0.2 and 24 Hz. The five remote stations

digitally transmitted the signals via a one-way VHF telemetry links to a central station Kislovodsk (KIV), where network-triggered data streams were recorded and initially examined.

A total of 1571 events were located from January 1992 to first half of 1994, of which 186 events were selected for study. Most of these 186 events are crustal, located at depths less than 30 km. Initially, waveforms were analyzed if: (1) the event was within 4° of the network so that *P* and *S* waves were well defined, (2) at least four phases were recorded at least by three stations for the location, (3) the signal-to-noise ratio of main arrival to pre-event noise was greater than 3, and (4) there were no telemetry gaps in recording. Data for 1992 were picked and associated by the Joint Seismic Program (JSP) Center (Harvey et al. 1994). For 1993 and 1994, the arrivals were picked visually using JSP software and events were located using locSAT (Bratt & Bache 1988). A total of 249 *P* and 304 *S* waveforms were used.

*Measurement of t**. Initial observations show that seismic waves propagate efficiently through platform paths, whereas high frequency signals become weaker for paths that cross mountain region (Figure 2). Hence, events used here were classified into two groups: those with ray paths that sample the Russian Platform (plusses in Figure 1) and those with paths that sample the Greater Caucasus mountains (solid circles in Figure 1). Frequency-independent attenuation parameters are measured by fitting body wave spectra $H(f)$ (e.g. Lees & Lindley 1994; Lindley & Archuleta 1992; Boatwright 1978) to

$$H(f) = \frac{\Omega_0 I(f) e^{-\pi f t^*}}{1 + (f/f_c)^2} \qquad (1)$$

where $H(f)$ is the Fourier displacement amplitude, f is the frequency, $I(f)$ is the known instrument response to ground displacement, Ω_0 is the frequency-independent term, f_C is the source corner frequency, t^* is the frequency-independent attenuation operator. The *P* and *S* arrivals are selected in a 2-5 s long window that contains the dominant energy, and their Fourier amplitude spectra are calculated by a multitaper technique (Park et al. 1987). *S* waves are rotated to the transverse orientation. For each record, a time window is chosen to include all direct arrivals and to encompass most of the initial arrival energies. Window length typically varies from 2 to 4 s for *P* waves and from 3 to 5 s for *S* waves, depending on epicentral distance. Tests showed that variations of t^* with window length are small and have no significant affect on *Q* measurements.

The log-amplitude spectra of *P* and *S* waves are fit in a least squares sense to $log[H(f)]$ to determine t^*, f_C and Ω_0 (Figure 3). The t^* values include several large outliers. In order to ensure robustness in inversion, we eliminate data if the t^* estimates are more than 3-σ from the mean value for each station. We assume t^* to be independent of frequency, probably reasonable over the relatively small (2-15 Hz) frequency of most of our measurements. For both *P* and S records, noise levels are determined from the spectrum of a window placed just prior to main arrivals. These noise measurements are used to determine the usable frequency band for each signal, limited to frequencies where the signal-to-noise ratio is obviously greater than 1. As well, frequencies below the instrument natural frequency, 0.2 Hz, are not used. Typical frequency ranges are for *P* waves is 1-15 Hz, and 1-12 Hz for *S* waves.

In the initial t^* measurements, the f_C for a single event varies widely between stations, perhaps because t^* estimates trades off with f_C. In order to understand any possible systematic correlation between these parameters, t^* is estimated twice: once by constraining f_C to a single value for all records of the same event at different stations, and

once by allowing f_C to vary between stations. Results are similar (Table 1), indicating that the trade-offs do not significantly affect our results, a result also found by Lees & Lindley (1994). In all subsequent discussions, we present Q measurements from unconstrained f_C case which are based on more observations.

I.4 Path-averaged Attenuation

Initially, we separate the t^* measurements into two paths: platform paths and mountain paths. For each subset of t^* measurements we estimate a path-averaged attenuation operator, $\overline{Q}$ (e.g. Hough et al. 1988a) by

$$t^*(r) = t_0^* + \frac{r}{\overline{Q}V} \tag{2}$$

where t_0^* is the near-receiver contribution term, r is the distance. Here, V is the path-averaged velocity of relevant phases; 6.0 and 3.5 km/s for crustal P and S, respectively (Balavadze & Tvaltvadze 1958). The mantle P_n velocity is assumed to be 8.0 km/s, and 4.6 for S_n. For this simple model, $\overline{Q}$ and t_0^* are determined from linear regression of the $t^*(r)$ measurements (Table 1). We find that $\overline{Q}$ for mountain paths is two to three times lower than platform paths, and $\overline{Q}$ for P and S waves ($\overline{Q}_p$, $\overline{Q}_s$) are roughly equal (Figure 4, left).

At the five stations, t_0^* varies from 0.012 to 0.046 s for P waves and 0.016 to 0.051 s for S waves, values which are small but non zero. We interpret this parameter as the attenuation caused by lossy near-surface rocks. The t_0^* values are systematically larger for stations located on poorly consolidated sediments of the Russian Platform (NAG, MIC and KUB) than for mountain stations (KIV and GUM) (Table 1 and Figure 4, right), at least for S waves.

I.5 Inversion

In order to better understand the variations of observed t^* estimates, we modified the velocity inversion technique of Roecker (1993) to invert for Q^{-1}. The t^* estimates are related to Q^{-1} by

$$t^* = \int_{raypath} \frac{dr}{QV} \tag{3}$$

where the integral is taken along the ray path of seismic wave. Because t^* is linearly related to Q^{-1}, the inversion and error assessment here become much simpler than for velocity inversion. In practice we discretize the integral and assume that both Q and V are constant within small blocks.

Parameterization for Q^{-1}. Rather than present results for a single inversion with large numbers of free parameters, we invert t^* measurements for Q^{-1} in a sequence of increasingly complex parameterizations to test the significance of features of interest (Table 2). In all inversions, the attenuation grids are oriented N20°E so that one coordinate is parallel to the strike of the mountain. The medium is parameterized by blocks with constant Q^{-1} and constant velocity, but arbitrary shape, using the reparameterization scheme of Abers & Roecker (1991). Ray paths are calculated for each block by an approximate ray tracing technique similar to that of Thurber & Ellsworth (1980). In some inversions vertical variations in Q^{-1} are included by parameterizing velocity into three layers: a near-surface

layer (200 m thick), crust (45 km thick (Alexidze et al. 1993)) and upper mantle (below 45 km depth). In others, the Earth is assumed to consist of a single layer below the 200 m thick near-surface layer. The near-surface layer is included to mimic site-effects of soft sediments and is parameterized such that a separate block lies beneath each station. For both *P* and *S*, blocks that hit by at least four rays are kept for inversion.

Inversion and Constraints. For each phase (*P* and *S*), Q^{-1} is estimated using a linear inverse formalism of Tarantola & Vallette (1982). This formalism takes into account a priori uncertainties of data, model and theory, and allows a convenient and realistic way to estimate Q^{-1} along with its a posteriori uncertainty (formal error) and resolution. The solution has the standard form

$$\boldsymbol{m} = \boldsymbol{m}_o + [\boldsymbol{G}^{\mathrm{T}}(\boldsymbol{C}_{dd} + \boldsymbol{C}_{tt})^{-1}\boldsymbol{G} + \boldsymbol{C}_{mm}^{-1}]^{-1}\boldsymbol{G}^{\mathrm{T}}(\boldsymbol{C}_{dd} + \boldsymbol{C}_{tt})^{-1}(\boldsymbol{d}_{\mathrm{obs}} - \boldsymbol{G}\boldsymbol{m}_o) \qquad (4)$$

where $\boldsymbol{m}$ is the estimate of model parameters, $\boldsymbol{m}_0$ is an a priori estimate of $\boldsymbol{m}$, $\boldsymbol{G}$ is the matrix of partial derivatives of t^* with respect to model parameters, $\boldsymbol{C}_{dd}$ is the a priori covariance matrix of the data vector $\boldsymbol{d}$, $\boldsymbol{C}_{mm}$ is the a priori covariance matrix of $\boldsymbol{m}$, $\boldsymbol{C}_{tt}$ is the a priori covariance matrix of the theoretical uncertainty. Assuming uncertainties of data, model and theoretical errors are independent and uncorrelated, the corresponding covariance matrices $\boldsymbol{C}_{dd}$, $\boldsymbol{C}_{mm}$ and $\boldsymbol{C}_{tt}$ are constructed as diagonal with individual elements being σ_d^2, σ_m^2 and σ_t^2, respectively.

The term σ_m and $\boldsymbol{m}_0$ reflects a tie between the resultant model and a priori estimate of the model. We fix $\boldsymbol{m}_0$ of 0.02 (Q=50) for 200 m thick near-receiver layer and 0.001 (Q=1000) for lower layers. The a priori uncertainties (σ_m) are set equal to $\boldsymbol{m}_0$ in each block. The a priori uncertainties of data (σ_d) are set to the standard errors calculated for t^* estimates, and are typically in the range of 0.002 - 0.007 s for both *P* and *S* waves. Also, we fix σ_t=0.01 s, the same order of magnitude as the t^* estimates, as a crude estimate of uncertainty due to incompleteness of the parameterization.

Source depth effects. For events that are well outside the network, source depth is poorly constrained. When coverage is good, the best located earthquakes in this region are no deeper than ~15 km (Triep et al. 1995), so it seems reasonable to assume that all Caucasus events lie in the upper crust. (Some hypocenters used in the present study are placed by location programs at ~100 km depth, where continental lithosphere is believed to have little strength. These events are several hundred km outside the network and the depths are probably erroneous.) Although source depth is weakly constrained, for events outside of the network, the actual depth has little effect on Q measurements. A series of inversions (not shown) were conducted in which all event depths are constrained 1, 5, and 20 km. Residual variances do not show any significant change between these inversions (*P* <3%; *S* <1%), and Q^{-1} values are similar within their formal uncertainties. Hence, reasonable depth uncertainties will not grossly affect Q^{-1} estimates.

I.6 Results

The increasingly complex sequence of inversions (Table 2) show trade-off between residual variance and the number of free parameters (Figure 5). The variance decrease is less than 1% between final inversion shown (parameterization *J*, Figure 6) and most complex parameterization attempted (parameterization *K*). The data variance in *J* is 0.609×10^{-3} s^2 for *S* and 0.341×10^{-3} s^2 for *P*, a ~60% reduction relative to the homogeneous half-space parameterization (*A*). For all inversions, the a posteriori error increases as size of block decreases. Uncertainties associated with Q_p^{-1} are 2-4× larger than Q_s^{-1}. Inversion results for Q^{-1} along with a posteriori errors are shown in map views and cross sections

for two different parameterizations *H* and *J* (Figure 6 and 7). For crustal blocks, resolution diagonals are >0.9 (Q_s^{-1}) or >0.84 (Q_p^{-1}). For mantle blocks ray coverage is sparser, and resolution diagonals vary from 0.48 to 0.99 (Q_s^{-1}) or 0.36-0.96 (Q_p^{-1}).

From these tests, two aspects of parameterizations emerge as being responsible for most of the variance reduction: allowing different Q^{-1} values beneath the mountains from those beneath the platform (parameterizations *C, D, F, H-K*), and including the near-surface "site effect" terms (*E-K*). Inversions that allow attenuation to vary across the strike of the mountains (e.g. parameterization *F*) shows that signals are roughly 2-3 times more attenuated beneath the mountains than beneath the platform region (for mountain paths Q_p^{-1} and Q_s^{-1} are $1.39 \pm 0.09 \times 10^{-3}$ and $1.36 \pm 0.06 \times 10^{-3}$, and for platform paths they are $0.58 \pm 0.07 \times 10^{-3}$ and $0.38 \pm 0.04 \times 10^{-3}$, respectively), and that Q_p^{-1} is roughly equal to Q_s^{-1} in each region. The corresponding residual variances of t^* are reduced by 20-30% from parameterizations that require lateral homogeneity (compare inversions *C, D*, and *F* with *A, B*, and *E* respectively). For both *P* and *S*, inversions that account for both lateral and vertical variations in Q^{-1} (parameterization *H* and *J*) show that attenuation contrasts between mountain and platform paths are similar to parameterization *F*, similar for both crust and upper mantle (Figure 6a and b (middle and bottom) and 7). Q^{-1} values for near-surface station blocks vary between 0.002 and 0.08, with the highest values seen at stations on soft and young sediments north of the network (Figure 6a and b, top).

The total variance reduction for inversion *J* is less than 5% relative to inversion *F*, the simplest to allow both near-station effects and lateral variation between mountains and platform. By comparison, variance reduces by more than 50% between inversions *F* and *A* (homogeneous half-space). The variance decrease is small between inversions that allow for separate upper mantle structures and those that do not, 6% (compare Model *G* and *H*), implying that the mantle structures are not well resolved. F-tests show that a lateral boundary between mountains and shield is required by the data, but further complexity is not.

Resolution. A synthetic data set of t^* values is inverted for Q^{-1}. The artificial data are calculated for a model with a single lateral step (Figure 8, top left), using all ray paths and uncertainties in the real data set. When inverted with parameterization (*H*), the correct Q^{-1} is recovered to within 10% in the crust and 14% in the mantle (Figure 8, top right). When inverted with a more complex parameterization (*J*), results depart from the correct values by up to 18% for crustal blocks, although the overall pattern is recovered (Figure 8, bottom). Mantle blocks vary more, up to 54%. The variance reduction gained by adding mantle blocks is less than 10%, because most of the ray paths are unaffected by the upper mantle structures. Resolution diagonals are 30-40% lower for mantle blocks relative to simpler inversions. For all blocks, the deviations between true models and that determined by the inversion are less than 1-σ formal errors. This suggests that the formal error estimates may overestimate true uncertainties by several times, although several sources of error, such as error associated with incomplete parameterization, are not modeled in this test.

Boundary Between High-Q and Low-Q regions. The boundary between high-*Q* and low-*Q* regions is sharp and closely follows the northern foothills of the mountains. The location of this boundary is evaluated by performing inversions repeatedly for parameterizations with a single lateral *Q* step, similar to parameterization *F*, but moving the location of the boundary north and south (Figure 9b). For each inversion, the residual variance is calculated. Based on this variance reduction, for both *P* and *S* the location of the boundary is constrained at 43.67°E longitude to lie at 43.265°N latitude, along the lower foothills of the northern slope of the Greater Caucasus. The 95% confidence limits (*F* test)

on N-S boundary location are 80 km wide for S and 130 km wide for P waves (Figure 9a). Hence the boundary is beneath the northern foothills, where surface geology shows a simple monoclinal fold.

Depth sampling. Although the inversion results show similar Q^{-1} for the crust and upper mantle beneath the mountains and beneath the platform, it is unclear whether the present data can resolve upper mantle attenuation independently of that in the crust. Ray tracing shows that only a few ray paths (~12%) sample the upper mantle (although source depths are uncertain). The 6% variance reduction between inversions that include a separate crust and mantle (inversions *H, J*) and those that do not (inversions *F, I*) is statistically insignificant above a 90% confidence level, so Q variations with depth are not constrained by the present data set. The point is further illustrated by examining the windows chosen for initial t^* measurements. Examining the waveforms for paths between 1.8° and 3.5° distance (P_n-P_g cross-over distance is ~1.8°) shows that the selected time windows include both crustal (P_g, P_b) and mantle (P_n) phases (Figure 10). Spectral measurements will be dominated by the larger signal, which is typically P_g. Hence, it is reasonable to infer that the variations in Q^{-1} are best considered vertical averages of the entire crust.

I.7 Discussion

Attenuation values. Measurements made here are in the 2-15 Hz range, and can be compared to values determined in other regions at these frequencies. The Q values for the Russian shield (Table 1) are similar to those made in other stable cratons, while values from the Caucasus are typical of tectonically active regions. For example, several studies show that Q_S for eastern North America is near 2000 at 1-10 Hz frequencies (Atkinson & Mereu 1992; Boatwright 1994; Frankel et al. 1990), similar to the Russian shield values found here. Measurements from California show Q_P close to Q_S, near 800 at Loma Prieta (Fletcher & Boatwright 1991) or near 1000 at Anza (Hough et al. 1988a). The California values are similar to our estimates for attenuation beneath the Caucasus. A preliminary estimate for Q in the Kopet Dagh, near the Turkmenistan-Iran border, shows $Q_P \sim Q_S \sim$ 700, somewhat lower than values found in the Caucasus (Abers & Sarker 1996). Somewhat lower coda Q values for the Caucasus, Q_{coda} = 330 (Rautian et al. 1979), are made from 1 Hz coda measurements and may reflect differences in frequency and wave type.

I.7.i Attenuation Mechanism. In general, the causes of apparent attenuation are complex and include scattering by crustal heterogeneity, presence of cracks that are partially or fully saturated with fluids, and intrinsic dissipation (e.g. Mitchell 1995; Aki & Chouet 1975; Hough & Anderson 1988b; Frankel 1982). In many situations it is unclear that scattering and intrinsic mechanisms can be separated. However, some diagnostics favor intrinsic mechanisms for our observations. Overall, any feasible explanation of our data should account for several observations: (1) Q_s^{-1} and Q_p^{-1} are roughly equal (±11%) beneath the Greater Caucasus and beneath the Russian Platform; (2) for both P and S, Q^{-1} for mountain paths is 2-3 times larger than that of platform paths; and (3) a sharp boundary between high-Q and low-Q follows the northern foothills of the mountains.

Scattering. When a body wave propagates through a heterogeneous medium some high-frequency energy is lost to the wavefield coda by scattering (e.g. Wennerberg & Frankel 1989). Both scattering and intrinsic absorption contribute to observed Q of body waves. Energy conservation arguments and numerical simulations show that in a medium dominated by scattering, coda will be enriched in high frequencies relative to body waves

(Richards & Menke 1983; Frankel & Wennerberg 1987). By comparison, intrinsic attenuation represents a loss of energy at high frequencies throughout the seismogram.

To test for scattering, we compare the Fourier amplitude spectra of coda signals to those of the main body wave pulses for a small subset of events used in this study (Figure 11). Early coda spectra are measured in a time window that is 10-15 s delayed from the corresponding body wave arrival, and late coda spectra are measured at twice the *S*-wave travel time. The sharp spectral fall-offs seen for body waves sampling mountain paths are also seen the corresponding coda spectra, with similar spectral slopes. Such sharp high-frequency decays are not seen for shield paths. Hence it appears that both direct and coda signals propagating through mountains are attenuated similarly at high frequencies, a characteristic of intrinsic attenuation but not obviously a characteristic of scattering. It is less clear that Q for shield paths are dominated by intrinsic attenuation, as spectral fall-off is small below ~8 Hz for these paths, and fall-off in some cases is sharper for body waves than for coda (Figure 11). Hence, body-wave Q values (~2000) seen for the Russian shield conceivably could be dominated by scattering, but the low Q seen for mountain paths is more consistent with intrinsic attenuation.

Focusing. Q is determined here from spectral fall-off, so the only focusing effects of interest are those that produce variation in the 2-15 Hz frequency band. This requires structures that are of a size comparable to the relevant wavelengths (0.2 - 10 km). However, similar attenuation patterns are seen at all stations, over distances of 50-100 km, and sources within each tectonic province are distributed over several hundred km. The same focusing structure cannot be responsible for producing frequency-dependent effects along all of these paths. Some large-scale amplitude anomalies may be attributed to focusing effects of Moho structure (Cormier & Anderson 1996).

Cracks. At appropriate temperatures and degrees of saturation, the presence of cracks can lead to similar Q_s^{-1} and Q_p^{-1} (e.g. Mavko & Nur 1979), agreeing with our observation (1). These effects may be responsible for Q^{-1} patterns seen in some fault zones (Lees & Lindley 1994). However, it is unlikely that cracks will remain open at depths greater than 6-8 km (equivalent to ~0.20 GPa) (e.g. Jackson, Peterson & Fitz Gerald 1992; Christensen & Wepfer 1989). Most of the ray paths studied here are >100 km long and spend substantial time in the deeper parts of the crust or upper mantle, where open unsaturated cracks are unlikely. Cracks may contribute to attenuation within the near-surface layers (<200 m depth).

Anelastic Absorption. Most mechanisms of intrinsic attenuation depend upon temperature (e.g. Karato & Spetzler 1990; Anderson 1989), and high temperatures or partial melts have been considered as primary attenuation mechanism beneath several mountain belts including the Caucasus (e.g. Rodgers et al. 1997). Of the few laboratory studies that have been made at high temperatures and seismic frequencies, high-pressure experiments on dunites (Jackson et al. 1992) and room pressure experiments on basic rocks (Kampfmann & Berckhemer 1985) both show that Q_S and Q_P drop by a factor of 5-10 as temperature increases close to the solidus. Hence, large Q variations are viable without the presence of partial melts. At temperatures well below the solidus (e.g. <1000° C in dunites) attenuation appears to operate by a somewhat different mechanism than at higher temperatures, and shows an approximately linear (non-Arrhenius) relation between $log(Q^{-1})$ and temperature (Kampfmann & Berckhemer 1985; Jackson et al. 1992). Although individual studies show large differences in parameter values (see next section), in each case a factor of three attenuation variation as seen here can be easily explained by temperature variations well below the solidus.

Our observation that $Q_P/Q_S \sim 1$ differs from most deep-mantle observations, which show $Q_P/Q_S \sim 2$ (e.g. Karato & Spetzler 1990). Observations of $Q_P/Q_S \sim 2$ require that attenuation in shear ($Q\mu^{-1}$) be much larger than attenuation of bulk modulus (Qk^{-1}), consistent with several dissipative mechanisms (defect-based or grain-boundary based) likely to occur at high temperature. By contrast, $Q_P/Q_S \sim 1$ requires that $Q\mu^{-1}$ and Qk^{-1} be similar in size. The most likely mechanism to produce large Qk^{-1} is thermoelasticity, which is efficient in polycrystalline materials with grains that are anisotropic and have strongly varying thermal properties (Anderson 1989). It is easy to imagine that such conditions exist within metamorphic rocks common to continental collision zones, although little experimental evidence exists that quantifies Qk^{-1} and $Q\mu^{-1}$ in such rocks. As experimental measurements become available, the joint observation of Q_p and Q_s then may have value in constraining lower crustal composition.

I.7.ii Temperature beneath the Greater Caucasus. If the observed Q variations between shield and Caucasus mountains are entirely due to temperature, then these observations can constrain the temperature difference. At temperatures below 900° C, experiments on mafic and ultramafic rocks suggest that temperature (T) is related to attenuation by

$$T = 1100 - 150 f^{+0.06} \log_{10}(Q_s) \pm 50^\circ \text{C} \qquad (5)$$

(Kampfmann & Berckhemer 1985). Using this formula, our measurements made at frequencies of 2-15 Hz (Table 1) indicate temperatures of 520-580° C for shield paths and 590-650° C for mountain paths, for a temperature contrast of only ~70° C at any frequency (based on S wave $1000/Q$ values with unconstrained corner frequencies, Table 1). The shield temperatures are reasonable for values near Moho depths in old continents (e.g. Sclater, Jaupart & Galson 1981), consistent with our inference that the waves sampled mostly travel in the lower crust and uppermost mantle. The small temperature increase is insufficient to cause melting in mafic or ultramafic rocks.

Two factors temper our confidence in these numbers. First, the Q values for shield paths may be lowered by scattering (see above) and may represent an upper bound on temperature there. Second, the experiments made by Kampfmann and Berckhemer were made at room pressure, not at lower crustal conditions. In experiments at high pressures, Jackson et al. (1992) show a much larger factor of ten increase in Q^{-1} over the temperature interval 0° - 1000° C for dunite. Although they show that Q_s will equal 775 at temperatures below 600° C, a factor of 2.6 variation in Q_s (Table 1) would translate into a ~400° C temperature contrast between shield and mountains, about 5 times larger than predicted by Kampfmann and Berkhemer's experiments. Since the experiments of Jackson et al. (1992) were made in dunite and concentrated on near-solidus mechanisms their applicability to our setting is uncertain.

In conclusion, moderate temperature increases beneath the Greater Caucasus, sufficient to produce regional metamorphic effects, may explain the attenuation contrast. Although any direct association with temperature is not yet well constrained, small temperature variations are most consistent with our observations. The presence of Plio-Quaternary volcanism in parts of the Greater Caucasus shows that some melting must be occurring at depth, but it need not be widespread nor be the primary cause of the attenuation variations. Although most previous studies do not give quantitative Q values, it seems likely that previous observations of strong S_n attenuation beneath the Caucasus (e.g. Kadinsky-Cade et al. 1981; Rodgers et al. 1997) can be explained by elevated temperatures and not partial melt.

I.7.iii Geological Implications. Our results show high attenuation beneath high topography, with a sharp boundary that closely follows the northern foothills of the mountain ranges. Geologically, the boundary is represented by the active deformation front lies south side of the mountain ranges (e.g. Philip et al. 1989; Triep et al. 1995; Zonenshain & Le Pichon 1986). Surface geology also shows that the thrust sheets that characterize deformation on the southern slope are transported further south over adjacent massif (e.g. Dotduyev 1986; Philip et al. 1989). The inferred boundary at depth, thus, is north of the structural boundary at the surface, and underlies a region where surface geology shows only a simple monocline. In other words, high attenuation (Q^{-1}) is observed not just where faults are seen at the surface, but at depth where they project down dip.

If our inferences for the mechanism of Q^{-1} are correct, then some process is heating the mountain range throughout its extent. One speculative possibility is that convective instability within the mantle is elevating temperatures as a consequence of lithospheric thickening (e.g. Houseman, McKenzie & Molnar 1981). Such a mechanism would help explain the correspondence between inferred high temperatures and topography, unlike scenarios that appeal to high temperatures remnant from pre-Miocene subduction. Another possibility is that shear heating is significant at the downdip end of the active Greater Caucasus thrust fault systems (e.g. Figure 1), either through brittle faulting or through viscous dissipation in ductile shear zones. If the low P_n velocities observed by Hearn and Ni (1994) for the Caucasus as a whole coincide with the attenuation anomalies seen here, then that would suggest that the region of high temperatures extends too deep to be attributable to shear heating on faults. More work on the depth extent of structures needs to be done to test these possibilities.

High attenuation beneath the Greater Caucasus would cause densities to be anomalously low. As a consequence, some component of the high topography may be supported by Pratt-type mechanisms rather than by Moho deflections as is often assumed (Philip et al. 1989; Ruppel & McNutt 1990). For example, a temperature increase of 70 - 400° C throughout a 150 km thick lithosphere would generate 0.3 - 1.8 km of topography, for a coefficient of thermal expansion of $3 \times 10^{-5} \cdot K^{-1}$. One consequence is that the Bouguer gravity low over the Caucasus may not be a very good proxy for Moho depth changes. Unfortunately we know of no modern, direct measurements of crustal thickness beneath the Caucasus to test this speculation.

I.7.iv Implications for Regional Monitoring. No matter what the cause of Q^{-1}, the variations in signal behavior between mountain and shield paths has direct implications for use of body wave amplitudes in source discrimination and yield estimation. Similar variations in L_g and S_n amplitudes are seen for longer paths in the region (Abers, Kim & Lerner-Lam 1995; Rodgers et al. 1997). The sharp boundary between high-Q^{-1} and low-Q^{-1} regions suggests that the stations placed on the mountains suffer more attenuative loss of signal than those on the nearby shield. More importantly, smooth attenuation models such as those based upon long-period surface waves probably alias attenuation changes across major tectonic boundaries. Such sampling problems are significant for paths that lie within a few hundred km of the boundary. Propagation across such short paths could play an important role in verifying the Comprehensive Test Ban Treaty, as the characteristics of signals generated by small events come under increasing scrutiny.

I.9 Acknowledgments. We thank A. Lerner-Lam, D. Lentrichia, and several others at Lamont, as well as O. Starovoit, O. Isai, and many others in Kislovodsk and Obninsk for ensuring the quality of the Caucasus network data. Data processing for 1992 was largely done by D. Harvey at the J.S.P. Center, and all data were made available through the IRIS DMC. Collection of data was funded at Lamont by the IRIS Joint Seismic Program. Analysis was funded by AFOSR Grant F49620-95-1-0002.

II. Long Path Data Analysis.

Summary. As part of this project we extract a set of waveforms suitable for long-path analysis from the Caucasus Network (CNET) data set. Because the primary recording was on short (~3 minute) triggered windows, late phases were missed on many seismograms for path lengths >5° and some events were not recorded at all. A secondary, backup set of continuous data tapes were uncovered and decoded to provide long records for these events. The strategy was to search for records corresponding to all Iranian Plateau events identified in the PDE catalog. From the time period of operation, 20 events over 6 months of recording were in the PDE catalog and derivable in this way (Figure 12). These records demonstrate several aspects of the Caucasus network recording and contemporaneous Geyokcha array recording. In particular, (1) the CNET triggering algorithm only "missed" 1 of 20 events that had visible signals at >0.2 Hz, due to a month-long triggered data outage; (2) *Lg* is absent and *Sn* is only present at frequencies < 1 Hz on paths > 1000 km at both CNET and Geyokcha; (3) detection is poor for Zagros events with magnitudes < 4.5 from either of these sites (10 - 18° range); and (4) surface waves at ≤ 0.1 Hz may provide additional useful signal. These results suggest that detection of small events is difficult along these paths, and that *Sn/Pn* discriminants here need to be carefully designed around the optimal frequencies of propagation.

II.1 Caucasus Network

The Caucasus network was established in 1991 through the Joint Seismic Program, as a cooperative project between Lamont-Doherty and the OME-Obninsk group (Abers, 1994). The network, based in Kislovodsk (KIV), consists of 5-6 digitally telemetered 3-component sensors with 0.2 Hz natural periods, digitized at 60 sps (Figure 1). These stations are on the north side of the Greater Caucasus range, and straddle the transition from the Russian Shield to the Caucasus collisional zone. The northern stations lie on flat-lying, poorly consolidated Neogene sediments, while southern stations lie on tilted, well-lithified Mesozoic sediments. The response of the Kinemetrics SV/SH sensors are well-suited for analysis of local and regional seismic waves, although prior to mid-1993 triggering windows usually did not include *S* or *Lg* for events farther than 10-15° from the network. We extracted seismograms from a continuously-recording backup system in order to produce a waveform data set suitable for these longer distances (Figure 13). Data for 1992 were picked and associated by the Joint Seismic Program Center (Harvey et al., 1994) and subsequent seismograms are distributed through IRIS. A total of 645 events were associated for 1992 (292 in the PDE), and 327 were associated with the PDE catalog in 1993.

II.2 Long-duration records for Zagros Events

Continuous recording backup tapes were generated at CNET from October 1993 to May 1994, as part of a network enhancement prior to shutdown. During this period 20 events occurred in southern Iran (in the Zagros mountains) that were listed in the PDE catalog. These events form the basis for this study.

Long-path records were retrieved from the continuous data stream for these 20 events. Of these events, 5 triggered the system and so the *P* waves were previously detected (Figure 14). The trigger algorithm appeared reasonably robust, as only one PDE events not included in the triggered data set showed any visible signal in the continuous data (> 0.2 Hz, in several frequency bands). That one event occurred during a 39 day period that the triggered stream was not archived (2/14/94 - 3/25/94). Thus, the triggering algorithm did not miss any visible events.

For comparison, these same 20 events were compared against the triggered data stream at the Geyokcha array in Turkmenistan. This array consisted of 12 broadband sensors deployed over a ~3 km^2 area, with supplemental geophone strings, locates in the Kopet Dagh foothills just north of the Iran border [*Pavlis et al.*, 1994]. The triggered stream only included one of the 20 events, with comparable signal-to-noise characteristics as observed at CNET. Following this observation we suspect that the observations at CNET would apply to any network or array on the northern margins of the tectonically active collision belts of central Eurasia, although quantitative observations have been made only at this one place.

These records confirm several patterns in wave propagation identified previously, and quantify them further. First, the *Lg* wave train is absent on paths crossing the Caucasus (although other studies show it present at the same stations for cratonic paths). Second, S_n is present, but only at frequencies of 0.5 Hz and lower. By comparison, previous workers report S_n being absent [*Kadinsky-Cade et al.*, 1981; *Rogers et al.*, 1997]. We suspect that those observations are a frequency-dependent property of wave propagation along these paths, and at least for the older studies a consequence of the 1 Hz natural frequency of analog Short-Period sensors. In fact, at 0.25 Hz *Sn* is the dominant phase on the seismogram and P_n is only marginally visible (Figure 13).

A final observation is that only events larger than m_b 4.5 are detectable at 10-15° from CNET (Figure 14). This observation is not based upon a great number of points, but is consistent with the catalog analysis for 1992 made by *Harvey et al.* [1994] that suggests CNET under-detects the PDE at distances greater than 5° from the network. Again, comparison with records at the Geyokcha array suggest a comparable or slightly greater amount of attenuation for paths to the Kopet Dagh, so we suspect that such attenuation is a common attribute of paths that traverse the Iranian Plateau. As a consequence monitoring along these paths alone will likely be insufficient to attain CTBT detection goals.

In summary, it appears that events of magnitude < 4.5 in southern and eastern Iran cannot be routinely detected near the Caucasus network. We confirm the absence of *Lg* along these paths, and better describe the behavior of *Sn*. The *Sn* phase group does exist but only at frequencies of 0.5 Hz or less. Discriminants based on *Sn/Pn* amplitude ratios may be possible for these paths but they would require careful attention paid to frequency of measurement.

III. Amplitude fluctuations along intermediate paths

Summary. Amplitudes of seismic waves recorded at the Caucasus network, along the north flanks of the Greater Caucasus, are measured and analyzed for attenuation characteristics. From one year of observation, 96 events between 1° and 10° from the network provide stable measures of RMS *Pn*, *Sn*, *Lg*, and late coda amplitudes. Measurements were taken from seismograms filtered at several narrow frequency bands centered from 0.5 to 8.0 Hz, where signal levels are highest. Our results confirm previously-inferred spatial variations in *Sn* and *Lg* attenuation, that the Greater Caucasus marks an abrupt boundary between the high-*Q* Russian Platform and a region of exceedingly poor *Sn* and *Lg* propagation within the collision belt. Paths that cross large Quaternary volcanic provinces, along the Greater Caucasus, seem most affected. Amplitude

ratios show the largest regional differences in the 1-2 Hz range and decrease at higher frequencies, and indicate complicated changes in the mechanism of attenuation between shield and tectonic paths.

For a given path the RMS amplitudes of the *Lg* group and late coda phases predict magnitudes as well as can be expected from *mb* uncertainties. However biases of 1.0-1.5 magnitude units are seen for RMS amplitudes along different paths, at frequencies higher than 1 Hz. Variation is much reduced by taking 3-component and network averages of amplitude measurements.

III.1 Introduction

Severe changes in wave behavior are observed between paths that cross the Caucasus and other Alpine-Himalayan mountain belts, and those that do not (Figure 15). These changes represent substantial attenuation of phases often used to discriminate explosions from earthquakes and to estimate event size and type, such as *Lg* and other high-frequency surface-related phases. In this study we analyze phase amplitudes for events within 10° of the Caucasus Seismic Network (CNET). Other facilities, such as the Geyokcha, Turkmenistan array also provide digital seismograms that give complementary information.

III.2 RMS Amplitudes of Regional Phases

We have measured RMS amplitudes of *P*-group, *S*-group, *Lg* and similar, and late coda from recordings of events 1-10° from CNet. Because the CNet time series contain occasional spikes and, at some stations, frequent telemetry gaps, routine and automated spectral methods are often problematic. More robust amplitude estimates are made from RMS amplitudes of multiple-narrow-band signals. For each seismogram, a series of narrow-band filters are constructed and applied centered at 0.5, 1.0, 2.0, 4.0, and 8.0 Hz. For each channel and frequency, RMS amplitudes are made in several time windows: pre-event noise, *Pn*, *Sn*, *Lg*, and coda. *Pn* and *Sn* windows extend from 4 s before the predicted phase onsets to 0.25 times the *S-P* time past the onset, up to 25 s in total length. The so-called *Lg* window covers the period in group velocity between 3.6 and 2.6 km/s; the range extends to slower than normal group velocities to include the dominant slow short-period surface phases observed for shield paths (Figure 15). The coda window is centered at twice the *S* travel time after the origin time, and is 40 s in duration. Only segments that were more than 4 s long are used, and only those where dropouts constituted less than 10% of the time window. These requirements allow some data where short trigger-windows or occasional dropouts might be present, and because the RMS measurements are integrated quantities the measurements are still valid. All seismograms are visually culled for other, unusual problems.

An RMS combination is made of measurements from each 3-component seismogram set, for as many components as were usable. Signal-to-noise estimates are made on these combined sets, and records with low (<2) signal level signals are eliminated. Noise estimates are made from each filtered seismogram, where possible, or instead taken as the maximum observed RMS noise level for a particular channel and frequency. Amplitudes are corrected in an RMS sense for incoherent noise contamination. Finally, amplitudes are averaged geometrically across the network for each event (and across all events for each station) to give a network-average set of amplitude ratio estimates. Only averages of three more stations are kept. These averages were considerably less variable than single station estimates.

III.3 Results

In map view (Figure 16) large variations in amplitude ratios are seen between paths that cross the crest of the Greater Caucasus and those that do not, and indicate extensive *Lg* blockage and *Sn* attenuation throughout the actively deforming parts of the Caucasus belt. Such behavior was seen by Kadinsky-Cade et al. [1981], although they did not have access to stations north of the Caucasus and were limited to analog records. Using some of the same Caucasus Network data Rodgers et al. [1994, 1997] saw a region of poor *S* and *Lg* propagation beneath the Caucasus. Our results document the frequency dependence of this phenomenon, and (similar to Rodgers et al.) show that the boundary of the attenuative region is sharp and lies beneath the core of the Greater Caucasus. Results are most consistent for the *Lg* window although the *Sn* window behaves similarly. Differences are most pronounced at lower frequencies (Figure 17).

Paths from events in the Dagestan-Chechnya region (DA, Figure 17, 18) are roughly parallel to the strike of the ranges and follow the margin of the mountains and traverse thick foredeep sediments north of the Greater Caucasus. These paths are also characterized by slow (~2.9-3.0 km/s) high-frequency Rayleigh waves (Figure 15). Large amplitudes are seen most frequencies, particularly from 0.5 to 2 Hz, and may reflect the a layered, relatively undisrupted nature of the paths.

Paths that cross the Greater Caucasus show very low-amplitude *S* and *Lg*-related phases relative to the *P* arrivals, even for relatively short paths. Many events are roughly 200 km distant, near the 1991 Racha earthquake zone (Triep et al., 1995), yet show amplitude ratios 3-10 times lower than for Dagestan paths. Waves from these events traverse the active deformation front of the Greater Caucasus, and the region of Plio-Quaternary volcanism near Mt. Elbruz at the SE edge of the network. Paths from events farther south that traverse the Lesser Caucasus show very small-amplitude late phases.

Absolute RMS amplitudes for a given region correlate well with event size measures such as m_b (Figure 18) although the scaling parameters vary systematically between regions. The m_b values come from the PDE for region TU, and from the CNet Information Product for closer events (so that some coupling with RMS *Pn* is expected). In general correlation coefficients are 0.8-0.9 for each population between 1 and 4 Hz. Events from Turkey show RMS amplitudes of late phases a factor of 10-100 low at 2 Hz compared with shield paths, with the discrepancy increasing with frequency. Some of the best correlations (>0.9) come from late coda amplitudes, which have long been used for magnitude determination in the Caucasus (Rautian et al., 1979). The variation from region to region corresponds to biases of 1.0-1.5 magnitude units in the ability of 2-Hz *Lg*, *Sn*, or coda to predict *mb*.

Variation is also seen between stations consistently for all events (not shown). The stations farthest onto the platform show consistently large *Lg/Pn* and *Sn/Pn* amplitude ratios by a factor of 1.7-2.5 relative to stations at high elevation, as well as the largest absolute amplitudes. The large amplitudes can be attributed to low velocities of Neogene near-surface sediments that lie beneath the platform stations.

Conclusions and Recommendations

I. We have shown that spectral fall-off of seismic body waves at 2-15 Hz can constrain attenuation through the Greater Caucasus and through the Russian Platform. Overall, signals are 2-3 times more attenuated beneath the mountains relative to the adjacent shield. Three-dimensional inversions of t^* measurements confirm these observations and demonstrate that the boundary between high-Q and low-Q regions is sharp and closely follows the northern slope of the mountain front. The location of this inferred boundary is somewhat different from that of surface deformation front, which lies on the southern slope of the mountains. Comparison of body wave with coda behavior suggests that intrinsic

attenuation, not scattering, is responsible for most of the difference between mountain and shield paths. Scant laboratory observations on Q -temperature relations imply 70-400° C higher temperatures at the base of the crust beneath the mountains relative to the platform. These temperature increases are not obviously high enough to trigger partial melting, although some localized melting beneath the Elbruz volcanic region must occur. On the other hand, if the inference of elevated temperatures is correct, then a significant fraction of the topography of the Greater Caucasus may be supported by decreased density rather than by crustal thickening.

Regardless of the mechanism, our results show that attenuation variations associated with Alpine-Himalayan mountain belts are large and can be abrupt. Any attempts to use amplitudes of regional phases propagating near and through these and similar mountains, such as for treaty verification purposes, need to trace raypaths carefully in order to properly account for the sharpness of these boundaries. The Q^{-1} values derived here should be useful in calculating or correcting amplitudes of seismic signals traversing this region.

II. Extreme attenuation beneath the Iranian Plateau limit the utility of high-frequency waveforms at ranges of 5-15°, for sources smaller than M ~ 4.5. Phases such as *Lg* are absent, and the *S* wave train is only apparent at frequencies of 0.5 Hz. Reliable detection of signals is likely to require a combination of *P* waves near 1 Hz, *Sn* near 0.25-0.5 Hz, and longer-period surface waves. Discrimants are possible based on *Sn/Pn* ratios, but likely *Sn* measurements need be made at frequencies of 0.2 - 0.5 Hz while *Pn* can be made at 0.5 - 2 Hz. No signals were detected at frequencies higher than 4.0 Hz for paths > 10°, from Zagros events to Caucasus (or Kopet Dagh) stations. Future work should include the analysis of longer period surface waves as a signal discriminant along such paths, not possible with the instrumentation in place for the CNET experiment.

III. Reduction in high-frequency seismic wave amplitudes across Eurasian collision zones appears to be associated with a highly localized boundary that follows the northern margin of the Greater Caucasus. Events in the Racha region, on the southern flanks of the Greater Caucasus, show reduction in *Lg/P* and *S/P* amplitude ratios comparable to more distant events that cross the entire region. Although amplitude ratios seem stable for paths from individual regions, as evidenced by the good correlations with m_b, the attenuation effects are highly variable. A spatially-varying attenuation model for the region is necessary in order to utilize *Lg/Pn* and *Sn/Pn* discriminants as these amplitude ratios vary by over a factor of 5-20 between different paths. The amplitude reduction, seen throughout the 0.5-4 Hz band, suggests that signals will be small for small regional events in the Caucasus-Iranian Plateau region, relative to comparable paths along shield sites. Robust measurements seem to require both 3-component analysis and averaging over several nearby stations, both done here. Future work should include quantifying frequency-dependent Q in a way that can be used for path calibration, and adding complementary observations from other networks and arrays.

REFERENCES CITED

Abers, G.A. & Roecker, S., 1991. Deep structure of an arc-continent collision: earthquake relocation and inversion for upper mantle P and S wave velocities beneath Papua New Guinea, *J. Geophys. Res., 96*, 6379-6401.

Abers, G.A. & Sarker, G., 1996. Seismic sources and structure in Iran and the Caucasus from Joint Seismic Program array data: Attenuation variations at the northern margins of Eurasian mountains, in *Proceedings of the 18th Annual Seismic Research Symposium,* 4-6 September 1996, Annapolis, Maryland, PL-TR-96-2153, 1-9.

Abers, G.A., 1994. The Caucasus Seismic Network, *IRIS Newsletter*, 13, 16-17.

Abers, G.A., Kim, W.-Y. & Lerner-Lam, A., 1995. Seismic sources and structure in Iran and the Caucasus from Joint Seismic Program array data, in *Proceedings of the 17th Annual Seismic Research Symposium,* 12-15 September 1995, Scottsdale, Arizona, PL-TR-95-2108, 602-608.

Adamiya, Sh. A., Alekhidze, M.A., Balavadze, B.K., Gvantseladze, T.A., Kartvelishvili, K.M., Kuloshvili, S.I., Mindeli, P. Sh., Nazaretyan, S.N., Oganesyan, Sh. S., Radzhabov, M.M., Sikharulidze, D.I., Chelidze, T.L. & Shengelaya, G.Sh., 1992. Structure of the crust and upper mantle of the [former] USSR, *Int. Geol. Rev., 34*, 249-263.

Aki, K. & Chouet, B., 1975. Origin of coda waves: source, attenuation, and scattering effects, J. Geophys. Res., 23, 3322-3342.

Alexidze, M.A., Gugunava, G.E., Kiria, D.K. & Chelidze, T.L., 1993. A three-dimensional stationary model of the thermal and thermoelastic fields of the Caucasus, *Tectonophysics*, 227, 191-203.

Anderson, D.L., 1989. Theory of the earth, pp. 366, *Blackwell Scientific Publication*, Boston.

Anderson, J.G. & Hough, S., 1984. A model for the shape of the Fourier amplitude spectrum of acceleration at high frequencies, *Bull. Seismol. Soc. Am.*, 74, 1969-1994.

Atkinson, G.M. & Mereu, R.F., 1992. The shape of ground motion attenuation curves in Southeast Canada, *Bull. Seismol. Soc. Am.*, 82, 2014-2031.

Balavadze, B.H. & Tvaltvadze, G.K., 1958. The structure of the Earth's crust in Georgia according to geophysical data, *Izv. Geophys. Ser.*, 1075-1084.

Boatwright, J., 1978. Detailed spectral analysis of two small New York state earthquakes, *Bull. Seismol. Soc. Am.*, 68, 1117-1131.

Boatwright, J., 1994. Regional propagation characteristics and source parameters of earthquakes in Northeastern North America, *Bull. Seismol. Soc. Am.*, 84, 1-15.

Bratt, S.R. & Bache, T.C., 1988. Locating events with a sparse network of regional arrays, *Bull. Seismol. Soc. Am*, 78, 780-798.

Burtman, V.S., 1989. Kinematics of Arabian Syntaxis, *Geotectonics*, 23, 139-146.

Christensen, N.L. & Wepfer, W.W., 1989. Laboratory techniques for determining seismic velocities and attenuations, with applications to continental lithosphere, *Mem. Geol. Soc. Am.*, 172, 91-102.

Cormier, V.F. & Anderson, T., 1996. L_g blockage and scattering at CNET and KNET, in *Proceedings of the 18th annual seismic research symposium on monitoring a Comprehensive Test Ban Treaty*, 159-164, September 4-6.

DeMets, C., Gordon, R.G., Argus, D.F. & Stein, S., 1990. Current plate motion, *Geophys. J. Int.*, 101, 425-478.

Dotduyev, S.I., 1986. Nappe structure of the Greater Caucasus range, *Geotectonics*, 20, 420-430.

Fletcher, J. & Boatwright, J., 1991. Source parameters of Loma Prieta aftershocks and wave propagation characteristics along the San Francisco peninsula from a joint inversion of digital seismograms, *Bull. Seismol. Soc. Am.*, 81, 1783-1812.

Frankel, A. & Wennerberg, L., 1987. Energy-flux model for seismic coda: separation of scattering and intrinsic attenuation, *Bull. Seismol. Soc. Am.*, 77, 1223-1251.

Frankel, A., 1982. The effects of attenuation and site response on the spectra of microearthquakes in the northeastern caribbean, *Bull. Seismol. Soc. Am.*, 72, 1379-1402.

Frankel, A., McGarr, A., Bicknell, J., Mori, J., Seeber, L. & Cranswick, E., 1990. Attenuation of high-frequency shear waves in the crust: Measurements from New York state, South Africa, and Southern California, *J. Geophys. Res.*, 95, 17441-17457.

Gorshkov, G.P., 1984. Regionalnaya Seismotektonika Territorii Yuga SSSR: Alpiiskii Poyas (in Russian), *Nauka, Moscow.*

Gueguen, Y., Woirgard, J. & Darot, M., 1981. Attenuation mechanisms and anelasticity in the upper mantle, *in* Anelasticity in the earth, *ed.* Stacey, F.D., Peterson, M.S. & Nicholas, A., 69-79.

Harvey, D, and others, Caucasus Network Information Product Triggered events from January 1, 1992 to November 9, 1992, Version 1.0, IRIS-JSPC, 1994.

Hearn, T.M. & Ni, J., 1994. P_n velocity beneath continental collision zones: the Turkish-Iranian plateau, *Geophys. J. Int.*, 117, 273-283.

Hough, S. & Anderson, J.G., 1988b. High-frequency spectra observed at Anza, California: Implication for Q structure, *Bull. Seismol. Soc, Am.*, 78, 692-707.

Hough, S., Anderson, J.G., Brune, J., Vernon, F., Berger, J., Fletcher, J., Haar, L., Hanks, T. & Baker, L., 1988a. Attenuation near Anza, California, *Bull. Seismol. Soc. Am.*, 78, 672-691.

Houseman, G.A., McKenzie, D.P. & Molnar, P., 1981. Convective instability of a thickened boundary layer and its relevance for the thermal evolution of continental convergent belts, *J. Geophys. Res.*, 86, 6115-6132.

Humphreys, E.D. & Dueker, K.G., 1994. Physical state of the western U.S. upper mantle, *J. Geophys. Res.*, 99, 9635-9650.

Jackson, I., Peterson, M.S. & Fitz Gerald, J.D., 1992. Seismic wave dispersion and attenuation in Aheim dunite: an experimental study, *Geophys. J. Int.*, 108, 517-534.

Jackson, J. & McKenzie, D., 1984. Active tectonics of the Alpine-Himalayan belt between Western Turkey and Pakistan, *Geophys. J. R. Astron. Soc.*, 77, 185-264.

Kadinsky-Cade, K., M. Barazangi, J. Oliver, and B. Isacks, Lateral variations of high-frequency seismic wave propagation at regional distances across the Turkish and Iranian plateaux, *J. Geophys. Res., 86*, 9377-9396, 1981.

Kampfmann, W. & Berckhemer, H., 1985. High temperature experiments on the elastic and anelastic behavior of magmatic rocks, *Phys. Earth Planet. Int.*, 40, 223-247.

Karato S. & Spetzler, H.A., 1990. Defects microdynamics in minerals and solid-state mechanisms of seismic wave attenuation and velocity dispersion in the mantle, *Rev. Geophys.*, 28, 399-421.

Kim, W.-Y., 1987. Modeling short-period crustal phases at regional distances for seismic source parameter inversion, *Phys. Earth Planet. Inter.*, 47, 159-178.

Kovalev, G.N. & Masurenko, Yu.P., 1972. Present condition of Mount Elbrus volcano, *Int. Geol. Rev., 14*, 230-233.

Lee, D.K. & Grand, S.P., 1996. Upper mantle shear structure beneath the Colorado Rocky mountains, *J. Geophys. Res.*, 101, 22233-22244.

Lees, J.M. & Lindley, G.T., 1994. Three-dimensional attenuation tomography at Loma Prieta: Inversion of t* for Q, *J. Geophys. Res.*, 99, 6843-6863.

Lindley, G.T. & Archuleta, R.J., 1992. Earthquake source parameters and the frequency dependence of attenuation at Coalinga, Mammoth Lakes, and the Santa Cruz Mountains, California, *J. Geophys. Res.*, 97, 14137-14154.

Mavko, G.M. & Nur, A., 1979. Wave attenuation in partially saturated rocks, *Geophysics*, 44, 161-178.

Mitchell, B., 1995. Anelastic structure and evolution of the continental crust and upper mantle from seismic surface wave attenuation, *Rev. Geophys.*, 33, 441-462.

Mitchell, B., Xie, J. & Pan, Y., 1996. Attenuation and Blockage of L_g in Eurasia, *in* Monitoring a Comprehensive Test Ban Treaty, *ed.* E.S. Husebye and A.M. Dainty, 645-654.

Park, J., Lindberg, C.R. & Vernon, F.L., 1987. Multitaper spectral analysis of high-frequency seismograms, *J. Geophys. Res.*, 92, 12675-12684.

Pavlis, G., H. Al-Shukri, H. Mahdi, D. Repkin, F. Vernon, JSP arrays and networks in central Asia, *IRIS Newsletter, 13*, 9-12, 1994.

Philip, H., Cisternas, A., Gvishiani, A. & Gorshkov, A., 1989. The Caucasus: an actual example of the initial stages of continental collision, *Tectonophysics*, 161, 1-21.

Rautian, TG, VI Khalturin, and IS Shengeliya, Seismic coda envelopes and assessment of earthquake magnitudes in the Caucasus, *Phys. Solid Earth, 15*, 393-398, 1979.

Richards, P.G. & Menke, W., 1983. The apparent attenuation of a scattering medium, *Bull. Seism. Soc. Am.*, 73, 1005-1021.

Rodgers AJ, TM Hearn, and JF Ni, Pn, Sn and Lg propagation in the Middle East, *EOS Trans AGU, 75(44)*, 463, Fall, 1994.

Rodgers, A.J., Hearn, T.M. & Ni, J.F., 1997. Propagation characteristics of short-period S_n and L_g in the Middle East, *Bull. Seismol. Soc. Am.*, in press.

Roecker, S. W., 1993. Tomography in zones of collision: Practical considerations and examples, *in* Seismic Tomography Theory and Practice, *ed.* Iyer, H.M. & Hirahara, K., 584-611.

Ruppel, C. & McNutt, M., 1990. Regional compensation of the Greater Caucasus mountains based on an analysis of Bouguer gravity data, *Earth and Planetary Science Letters*, 98, 360-379.

Sclater, J.G., Jaupart C. & Galson, D., 1981. The heat flow through oceanic and continental crust and the heat loss of the earth, *Rev. Geophys. space Phys.*, 18, 269-311.

Tarantola, A. & Valette, B., 1982. Generalized nonlinear inverse problems solved using the least squares criterion, *Rev. Geophys.*, 20, 219-232.

Thurber, C.H. & Ellsworth, W.L., 1980. Rapid solution of ray tracing problems in heterogeneous media, *Bull. Seism. Soc. Am.*, 70, 1137-1148.

Triep, E., G.A. Abers, A. Lerner-Lam, V. Mishatkin, N. Zhacherenko, and O. Staravoit, Active thrust front at the south slope of the greater Caucasus: The 29 April, 1991 earthquake and its aftershock sequence, *J. Geophys. Res* , *100*, 4011-4034, 1995.

Wennerberg, L. & Frankel, A., 1989. On the similarity of theories of anelasticity and scattering attenuation, *Bull. Seismol. Soc. Am.*, 79, 1287-1293.

Winkler, K. & Nur, A., 1979. Pore fluids and seismic attenuation in rocks, *Geophys. Res. Lett.*, 6, 1-4.

Zhang, T. & Lay, T., 1994. Analysis of short-period regional phase path effects associated with topography in Eurasia, *Bull. Seismol. Soc. Am.*, 84, 119-132.

Zonenshain, L.P. & Le Pichon, X., 1986. Deep basins of the Black Sea and Caspian Sea as remnants of Mesozoic back-arc basins, *Tectonophysics*, 123, 181-211.

Zonenshain, L.P., Kuzmin, M.I. & Natapov, L.M., 1990. Alpine-Himalayan foldbelt within the USSR, Geology of the USSR: A plate-tectonic synthesis, *Am. Geophys. Un.,Washington, D.C.*, 167-179.

Publications Resulting from Project

Abers, G.A. and G. Sarker, Seismic sources and structure in Iran and the Caucasus from Joint Seismic Program array data: Attenuation variations at the northern margins of Eurasian mountains, in *Proceedings of the 18th Annual Seismic Research Symposium* 4-6 September 1996, Annapolis, Maryland, PL-TR-96-2153, pp. 1-9, 1996.

Abers, G.A., and L. Garinger, Estimating structure beneath IRIS array sites from teleseismic multichannel receiver functions, *IRIS Workshop 1996 Abstracts*, 73, Spring 1996 [Partly funded by other sources].

Abers, G.A., Array measurements and origins for phases used in receiver function calculations, *EOS Trans. AGU, 77*, F459-F460, 1996 [Partly funded by other sources].

Abers, G.A., W.-Y. Kim, and A. Lerner-Lam, Seismic sources and structure in Iran and the Caucasus from Joint Seismic Program array data, in *Proceedings of the 17th Annual Seismic Research Symposium* 12-15 September 1995, Scottsdale, Arizona, PL-TR-95-2108, p. 602-608, 1995.

Sarker, G, and G.A. Abers, Comparison of coda and body-wave measurements of high-frequency attenuation, in prep. for Bull. Seismol. Soc. Amer., 1997.

Sarker, G., and G.A. Abers, Deep structure along the boundary of a collisional belt: attenuation tomography of *P* and *S* waves in the Greater Caucasus, *Geophys. J. Int.*, submitted, 1997.

Sarker, G., G.A. Abers, and A. Lerner-Lam, Seismic Q and Regional Tectonism in the Greater Caucasus Continental Collision Zone, *EOS Trans. AGU, 76*, F353, 1995.

W.-Y. Kim, V. Aharonian, G. Abers, A. Lerner-Lam, and P. Richards, Discrimination of earthquakes and explosions in southern Russia using regional high-frequency data from IRIS/JSP Caucasus Network, in *Proceedings of the 17th Annual Seismic Research Symposium* 12-15 September 1995, Scottsdale, Arizona, PL-TR-95-2108, 68-77, 1995.

Figure Captions

Figure 1. The Caucasus. (top) Regional topography in gray shades, 500 m contour interval, network stations (solid triangles) along with telemetry links, and earthquakes used in Q measurements. Plusses denote events for platform paths; solid circles denote events for mountain paths. Other symbols: stars, Quaternary volcanoes (Philip et al. 1989); toothed lines, major thrusting of the Greater Caucasus (Philip et al. 1989; Triep et al. 1995); dashed lines, location of cross sections AA' and BB' (Figure 7 and 8). Inset shows location of study area. (bottom) N-S cross-section along AA', shown top. Also shown location of the network (CNET), major thrusting and sediments beneath the stations. E = volcanic center of Mt. Elbruz volcano; D = Dzhirula massif.

Figure 2. Vertical component seismograms recorded at station KIV, comparing regional phases between mountain and platform paths. Records are plotted in same scale. Numbers in parenthesis indicate group velocities in km/s. Although regional phases are efficient for the platform path, they are much weaker and longer period for the mountain path. Severe attenuation of high-frequency signals through the mountain paths may systematically bias body-wave magnitude estimates here. Event-distance (Δ) is approximately equal.

Figure 3. Example showing fitting spectra procedure to measure t^* for an event recorded at station GUM. (top) Seismograms from mountain path showing P and S windows along with pre-event noise, barred. (bottom) Spectra for P and S windows, labeled. Inverted triangle shows estimated f_C, and t^* values are shown in box. Main arrivals are solid lines, and noise curves are dashed.

Figure 4. (left) t^* estimates plotted against distance for mountain (o), "mnt", and platform (+), "plat", paths. Linear regression on $t^*(r)$ for events >0.25° gives the path-averaged Q values for each region, labeled. (right) Variation in t^* fitting of S for each station. Intercept t_0^* indicates near-receiver effect. Near-site attenuation is systematically higher for MIC, NAG and KUB, stations which lie on soft sediments. Station KNG has insufficient observations.

Figure 5. Variance (σ) reduction as a function of increasing parameterization complexity for both P (dashed) and S (solid) waves. The parameterizations are described in Table 2. Note different scales for P and S variances on either side of plot. The complexity of parameterization, essentially the number free parameters, increases to right. The improvement of model parameterization is achieved by adding a low-velocity layer beneath each station, and by allowing Q^{-1} to vary between mountain and platform regions (see text for details).

Figure 6. Results of attenuation inversions, (a) for parameterizations correspond to inversion H and (b) for inversion J. Each parameterization also shows number of free parameters (F.P.) that are solved in the inversion. Each block is labeled by Q^{-1} values, followed by formal errors (both multiplied by 1000). The depth range of each block is indicated on the top right of each panel. Triangles show station locations, and open squares are the Quaternary volcanic centers. Events used are shown in Figure 1. Q^{-1} for the topmost layer are 10-100 times larger than those for crust and upper mantle (gray scales are not shown). Q_p^{-1} for blocks deeper than 200 m is roughly equal to Q_s^{-1} in each region.

Boundary between high-Q and low-Q is sharp and closely follows the northern flank of the mountain.

Figure 7. Cross-sections (located on Figure 1) for parameterization *H* and *J*. Format similar to Figure 6. Actual topography is shown at the top of each cross-section, with 10× vertical exaggeration. Note high Q^{-1} beneath mountains.

Figure 8. Cross-section showing tests of resolution for Q_s^{-1}. (top left) Initial model used to generate artificial t^* measurements, corresponding to a single lateral Q step that varies with depth. Artificial data are generated for all events used in actual inversions. Normally distributed random noise is added, with variances equal to data uncertainties (calculated while determining t^*). Parameterizations and a priori uncertainties are similar to actual inversions. (top, right) Results for parameterization *H* and (bottom) for *J*. Format similar to Figure 6. Q_p^{-1} values are similar to Q_s^{-1} (not shown). Original Q^{-1} is recovered to within 18% for crustal blocks and 54% for mantle blocks, although the overall correct pattern remains same. In all cases, recovered Q^{-1} is less than 1-σ formal error from the correct value.

Figure 9. Test for the location of the boundary between high-Q and low-Q regions. (a) Topography along N20°E-S20°W profile and reduction in residual variances (σ) for t^*_p, t^*_s (labeled). Parameterization is similar to *F* (b), except the location of boundary is a free parameter. Inversion procedure is explained in text. For both *P* and *S*, the minimum residual crosses 43.265°N at 43.67°E (vertical dashed lines) along the northern foothills of the mountain. Double arrows on (a) show 95% confidence limits calculated from F-test statistics on residual variances. The corresponding attenuation contrast between platform and mountain is shown on (c).

Figure 10. Vertical records for a regional distant mountain event, showing that the selected time windows for t^* measurements (horizontal bars) are dominated by crustal signals (P_g and P_b). Hence, spectral measurements are also likely to be dominated by crustal phases. A Caucasus velocity model (Harvey et al. 1994) is used to identify P_n, P_b and P_g phases (dashed lines).

Figure 11. Spectral measurements comparing direct and coda waves, for one seismogram traveling a shield path (top, Δ=1.4°, back-azimuth=165°) and one traveling a mountain path (bottom, Δ=1.5°, back-azimuth=358°). The spectra of *S* and *S*-coda are calculated from transverse component seismogram, and *P* spectra are from vertical component records. Thick solid lines are the main arrivals; thin solid lines are the immediate coda, starting 10 s after onset of the main arrivals. Dotted lines on *P* panels (left) are pre-event noise; on *S* panels (right) dashed lines are coda spectra starting at twice the *S* arrival time (far coda). Triangles show the calculated source corner frequency for main arrivals. Note sharper fall-off of amplitudes for signals that traverse mountains than shield. Corresponding coda spectra also have the similar fall-off characteristics.

Figure 12. Map showing events from PDE catalog in Zagros, during period of continuous CNET recording. Open circles denote events that did not trigger, closed circles show events that did. Also shown is path to the one (of the 20) PDE events that triggered the Geyokcha array.

Figure 13. Examples of seismograms from 2 events in Zagros, recorded at one CNET station (NAG). The E-W component is shown to enhance *S* waves. Each panel shows the raw trace (bottom) and traces filtered in four narrow bands with center frequencies (from bottom to top) of 0.25, 0.5, 1.0, and 2.0 Hz. Note lack of Lg at all frequencies, and absence of *Sn* at frequencies below 0.5 Hz.

Figure 14. Magnitude versus source-receiver range for the 20 Zagros events in PDE catalog during the time CNET continuous records were collected. Each event is denoted by 2-3 circles, showing closest and farthest network station. Solid symbols showed detectable signal or resulted in an event trigger, while open symbols did not.

Figure 15. Records from two events from ~3° distance recorded at CNET. Waves for the upper event in Dagestan travel largely on the Russian Platform while waves for the Lesser Caucasus event, bottom, traverse the Greater Caucasus and Kura Basin. Seismograms are labeled by arrivals of *Pn, Sn,* and group velocities in km/s. Notice absence of late-phase energy on lower traces, particularly in and after Lg window (3.6 km/s). The upper event shows small *Pn* relative to *Sn* and late phases, and slow high-frequency surface waves (<3 km/s). Map, lower right, shows network configuration and event locations.

Figure 16. Ratios of RMS-Lg amplitude to P amplitude for events 1-10° from CNET, 1992. Each panel represents a different frequency bandpass, labeled top. Amplitude calculation is described in text. Symbols are centered on events and represent network-averaged amplitudes. Size of symbols scales to amplitude ratios according to key -- left-hand and right-hand numbers are for left and right column of figure, respectively.

Figure 17. Variation in RMS amplitude ratios as a function of frequency for three regions. Phases used are ratio of *Sn/Pn* (top) and *Lg/Pn* (bottom) for each of 3 subregions. Path lengths are 3 - 10°. Regions on Figure 18.

Figure 18. (left) Three-component RMS amplitudes of 2-Hz wave train vs m_b. Coda is 15-30 s window centered at twice the *S* travel time, *Lg* window spans 3.6 - 2.6 km/s group velocity, and *Pn* window extends to 25% of *S-P* time. Signal-to-noise ratios exceed 2.0 for all measurements, and measurements are averaged over 3 or more network stations. Different symbols correspond to regions: DA - Dagestan; RA - Racha aftershock zone; TU - Turkey. The m_b value is taken from PDE for TU and JSPC measurements elsewhere (Harvey et al., 1994). Correlation coefficients between log(amplitude) and m_b are shown in upper left of each plot. Amplitudes are corrected for cylindrical geometric spreading to nm/s at 100 km. (top right) Map of regions; GC = Greater Caucasus, LC = Lesser Caucasus, FSU = Former Soviet Union.

Figure 1

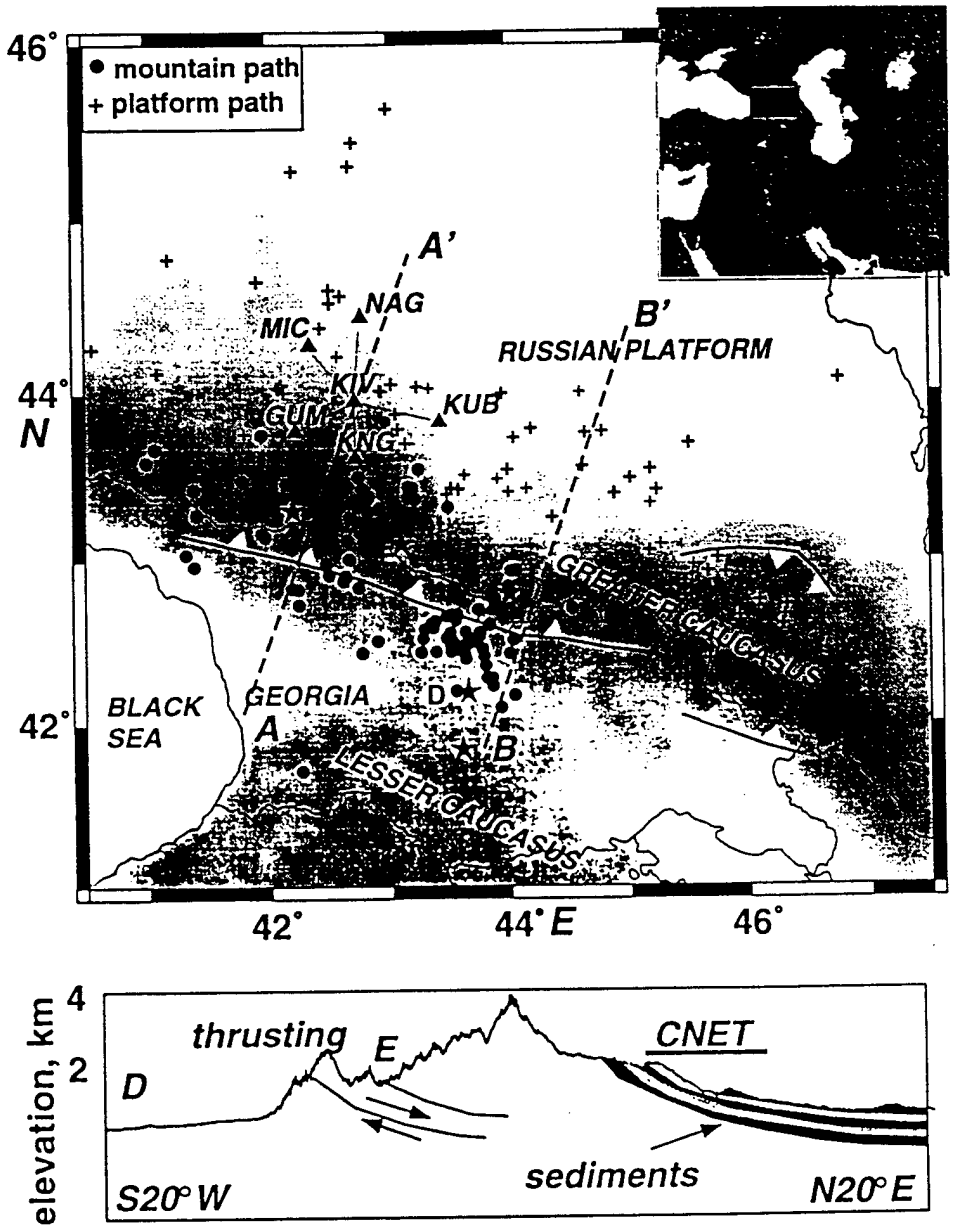
46°
● mountain path
+ platform path
A'
B'
NAG
MIC
KIV
KUB
GUM
KNG
RUSSIAN PLATFORM
44°
N
GREATER CAUCASUS
BLACK
SEA
GEORGIA
A
D
B
LESSER CAUCASUS
42°
42°
44° E
46°
elevation, km
4
2
thrusting
E
CNET
D
sediments
S20° W
N20° E

Figure 2

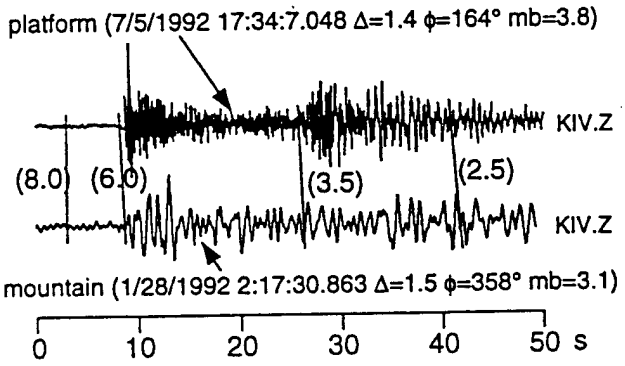
platform (7/5/1992 17:34:7.048 Δ=1.4 ϕ=164° mb=3.8)
KIV.Z
(8.0)
(6.0)
(3.5)
(2.5)
KIV.Z
mountain (1/28/1992 2:17:30.863 Δ=1.5 ϕ=358° mb=3.1)
0
10
20
30
40
50 s

Figure 3

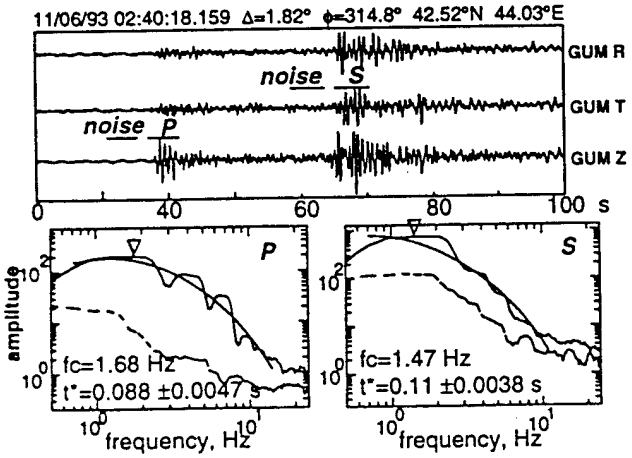
11/06/93 02:40:18.159 Δ=1.82° ϕ=314.8° 42.52°N 44.03°E
GUM R
GUM T
GUM Z
noise
S
noise
P
0
40
60
80
100 s
P
S
amplitude
fc=1.68 Hz
t*=0.088 ±0.0047 s
fc=1.47 Hz
t*=0.11 ±0.0038 s
frequency, Hz
frequency, Hz

Figure 4

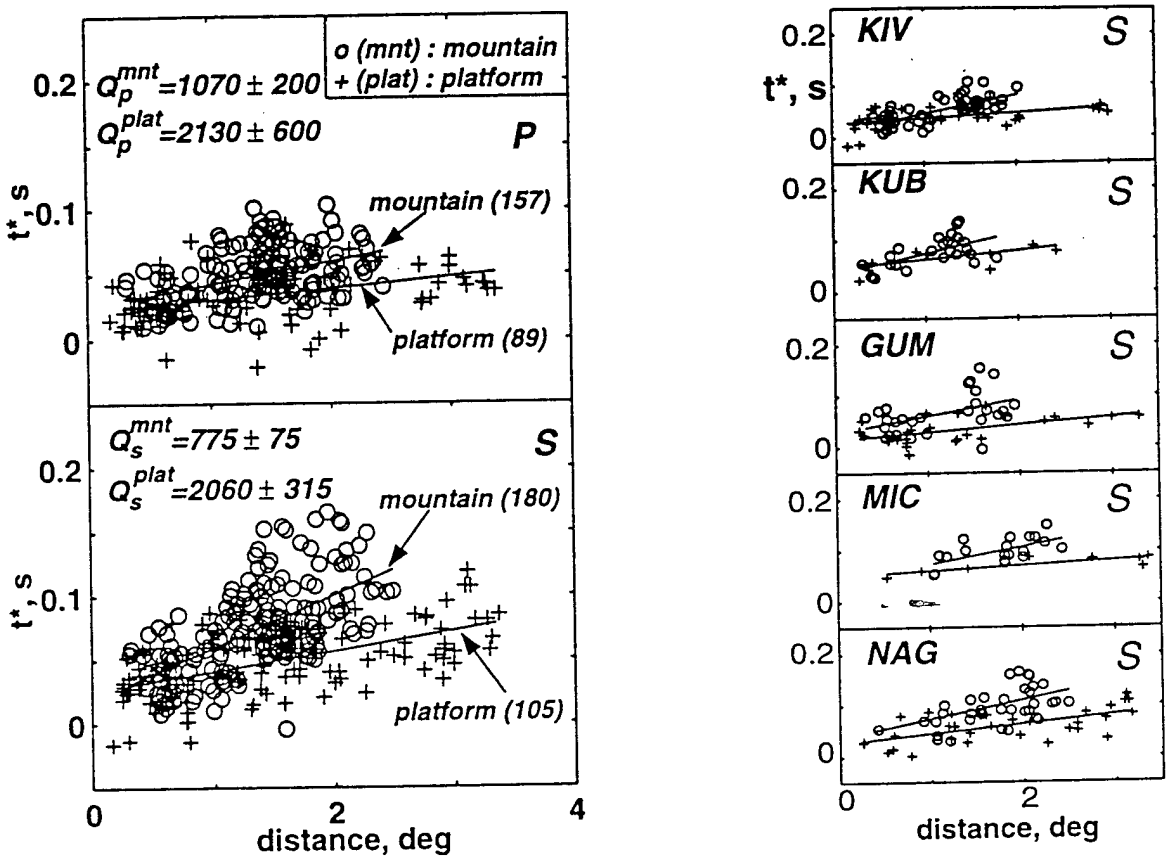
o (mnt) : mountain
+ (plat) : platform
Q_p^{mnt}=1070 ± 200
Q_p^{plat}=2130 ± 600
P
mountain (157)
platform (89)
Q_s^{mnt}=775 ± 75
Q_s^{plat}=2060 ± 315
S
mountain (180)
platform (105)
t*, s
0.2
0.1
0
0
2
4
distance, deg
KIV
KUB
GUM
MIC
NAG
S
t*, s
0.2
0
0
2
distance, deg

Figure 5

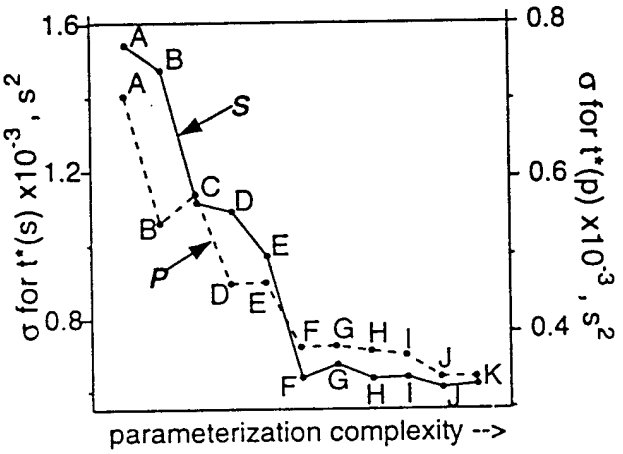
1.6
1.2
0.8
0.8
0.6
0.4
σ for t*(s) x10^-3, s^2
σ for t*(p) x10^-3, s^2
A
B
C
D
E
F
G
H
I
J
K
S
P
parameterization complexity -->

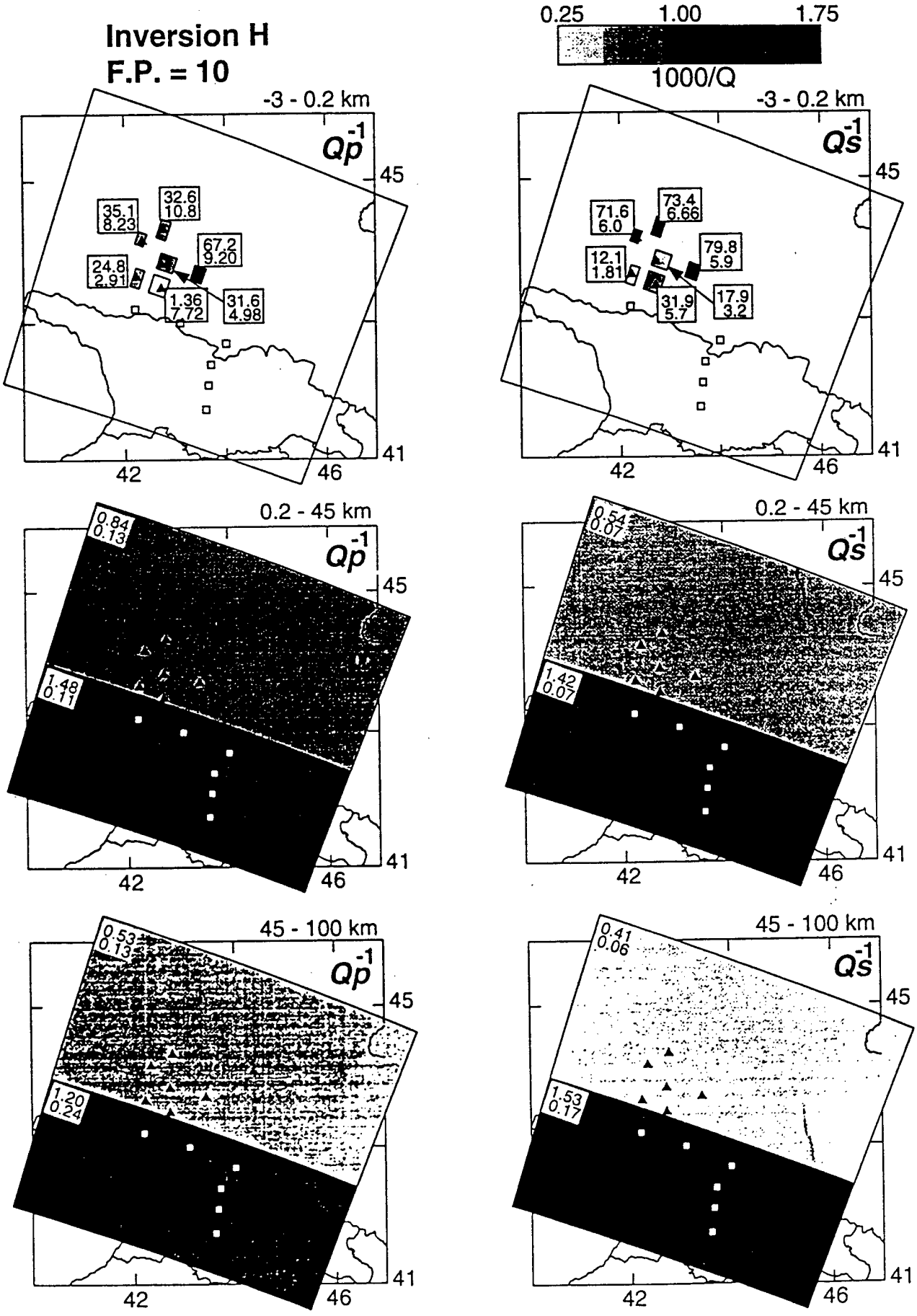
Inversion H
F.P. = 10
0.25
1.00
1.75
1000/Q
-3 - 0.2 km
Qp^{-1}
35.1
8.23
32.6
10.8
67.2
9.20
24.8
2.91
1.36
7.72
31.6
4.98
Qs^{-1}
71.6
6.0
73.4
6.66
79.8
5.9
12.1
1.81
31.9
5.7
17.9
3.2
0.2 - 45 km
0.84
0.13
1.48
0.11
0.54
0.07
1.42
0.07
45 - 100 km
0.53
0.13
1.20
0.24
0.41
0.06
1.53
0.17
45
41
42
46

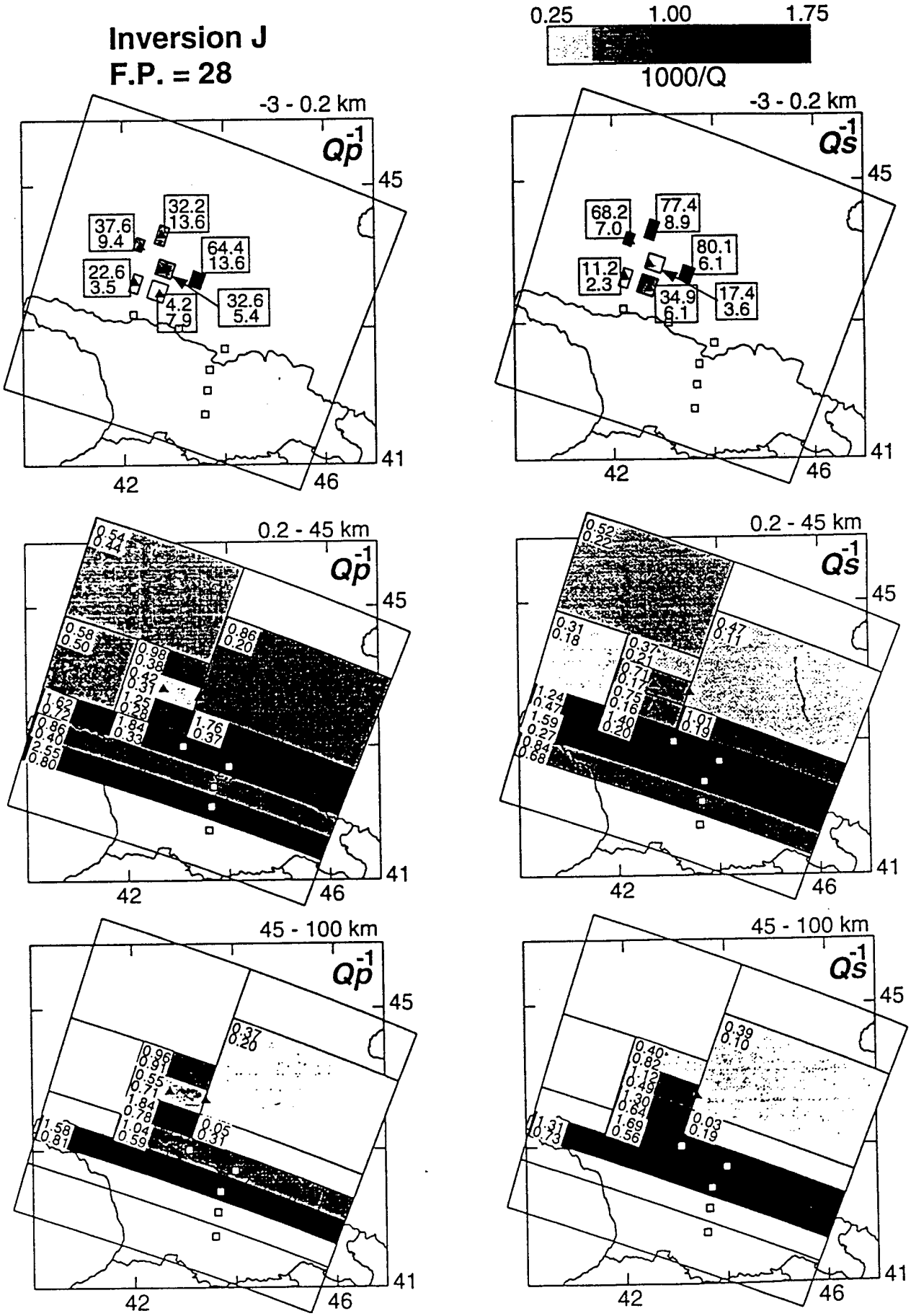
Inversion J
F.P. = 28
0.25
1.00
1.75
1000/Q
-3 - 0.2 km
Qp^{-1}
Qs^{-1}
0.2 - 45 km
45 - 100 km
45
41
42
46
32.2
13.6
37.6
9.4
64.4
13.6
22.6
3.5
4.2
7.9
32.6
5.4
68.2
7.0
77.4
8.9
80.1
6.1
11.2
2.3
34.9
6.1
17.4
3.6

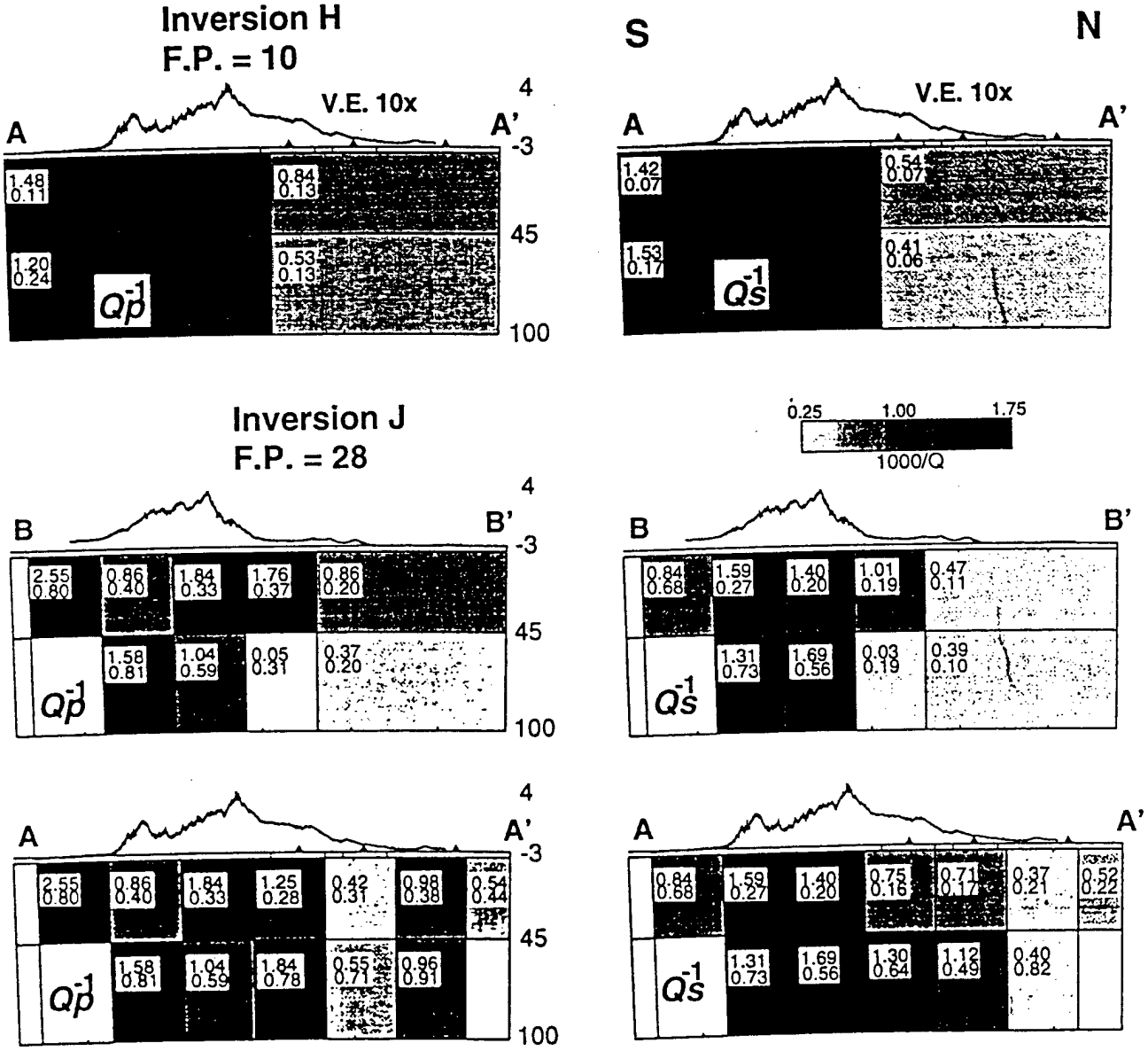
Inversion H
F.P. = 10
S
N
V.E. 10x
A
A'
B
B'
4
-3
45
100
1.48 0.11
0.84 0.13
1.20 0.24
0.53 0.13
Qp-1
1.42 0.07
0.54 0.07
1.53 0.17
0.41 0.06
Qs-1
Inversion J
F.P. = 28
0.25
1.00
1.75
1000/Q
2.55 0.80
0.86 0.40
1.84 0.33
1.76 0.37
0.86 0.20
1.58 0.81
1.04 0.59
0.05 0.31
0.37 0.20
0.84 0.68
1.59 0.27
1.40 0.20
1.01 0.19
0.47 0.11
1.31 0.73
1.69 0.56
0.03 0.19
0.39 0.10
2.55 0.80
0.86 0.40
1.84 0.33
1.25 0.28
0.42 0.31
0.98 0.38
0.54 0.44
1.58 0.81
1.04 0.59
1.84 0.78
0.55 0.71
0.96 0.91
0.84 0.68
1.59 0.27
1.40 0.20
0.75 0.16
0.71 0.17
0.37 0.21
0.52 0.22
1.31 0.73
1.69 0.56
1.30 0.64
1.12 0.49
0.40 0.82

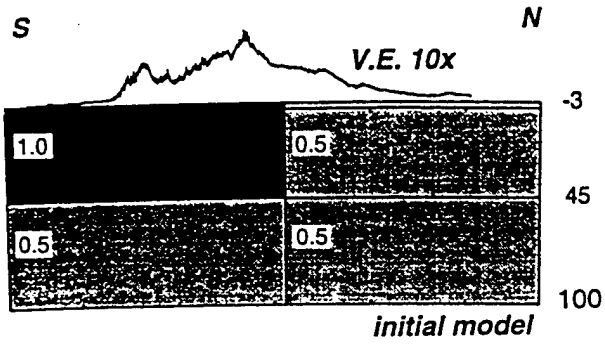

initial model

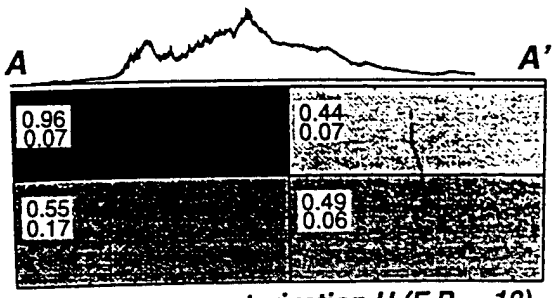

parameterization H (F.P. = 10)

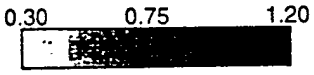

1000/Qs

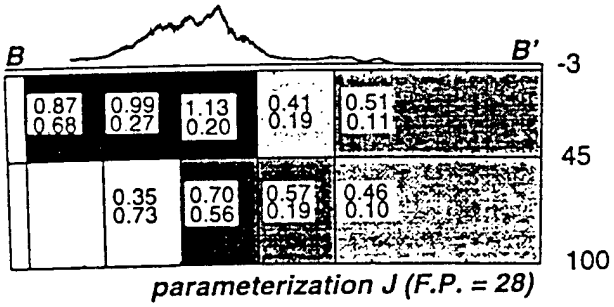

parameterization J (F.P. = 28)

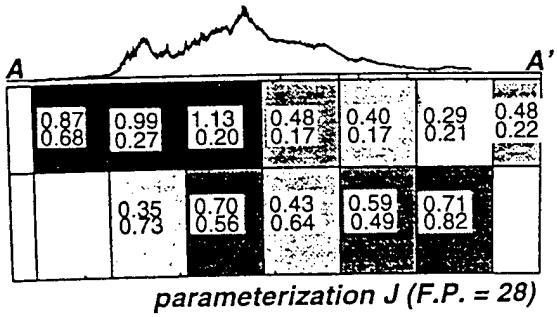

parameterization J (F.P. = 28)

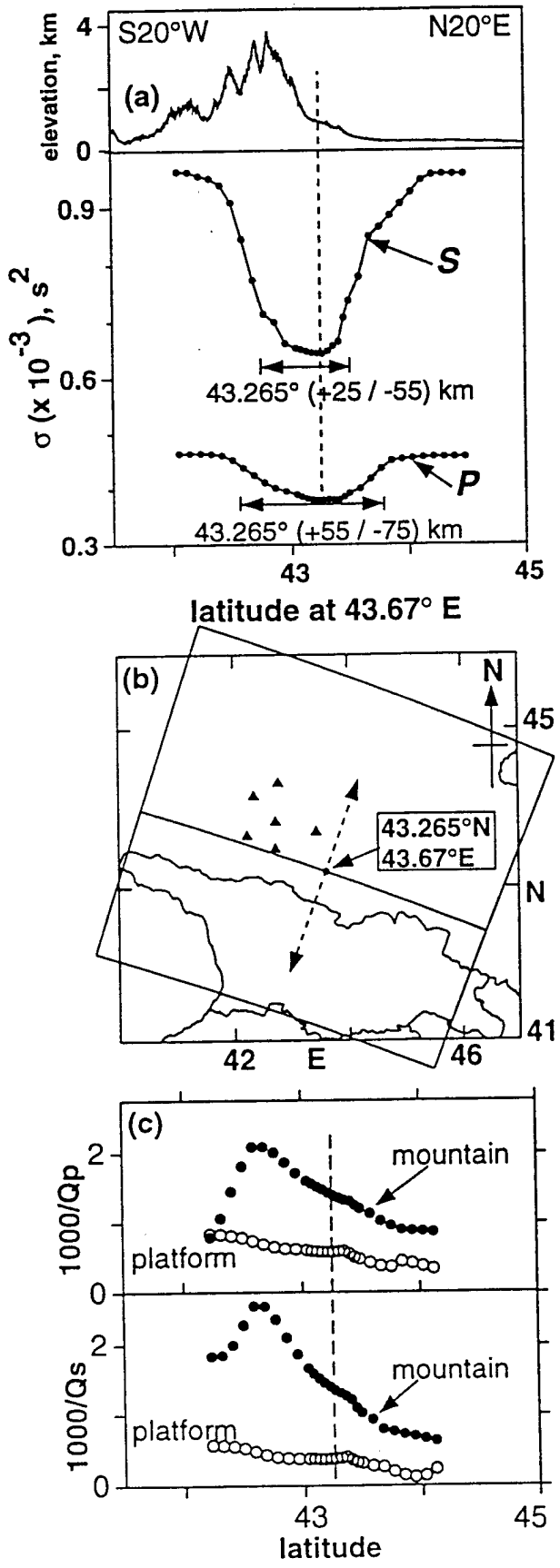
S20°W
N20°E
(a)
elevation, km
4
0
0.9
0.6
0.3
σ (x 10^-3), s^2
S
43.265° (+25 / -55) km
P
43.265° (+55 / -75) km
43
45
latitude at 43.67° E
(b)
N
45
43.265°N
43.67°E
N
41
42
E
46
(c)
mountain
platform
1000/Qp
2
0
mountain
platform
1000/Qs
2
0
43
45
latitude

Figure 10

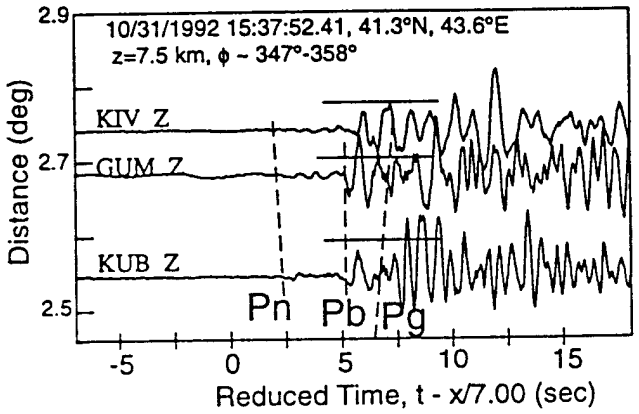
10/31/1992 15:37:52.41, 41.3°N, 43.6°E
z=7.5 km, ϕ ~ 347°-358°
KIV Z
GUM Z
KUB Z
Pn
Pb
Pg
Distance (deg)
2.9
2.7
2.5
-5
0
5
10
15
Reduced Time, t - x/7.00 (sec)

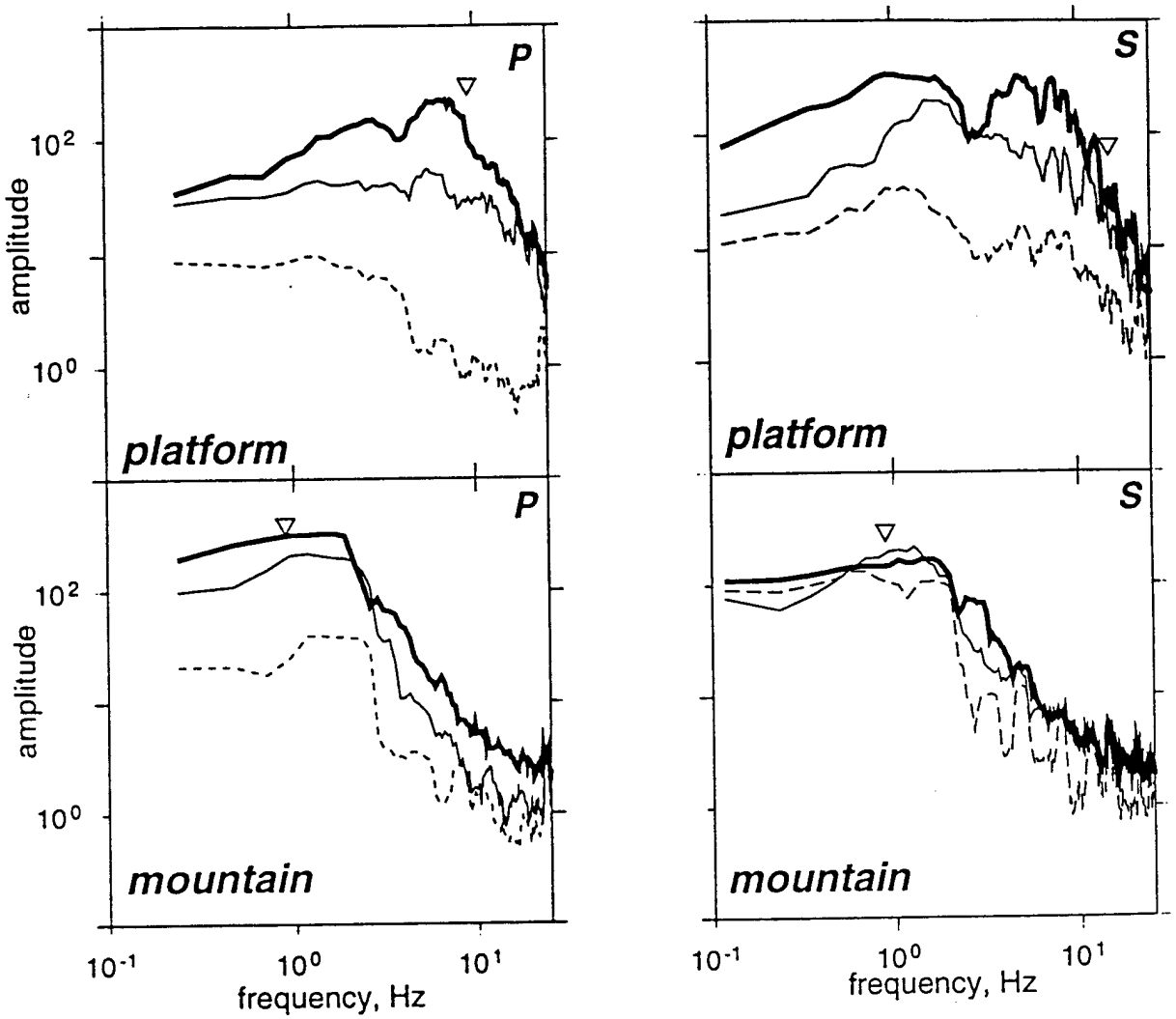
P
S
platform
platform
P
S
mountain
mountain
amplitude
amplitude
10^2
10^0
10^2
10^0
10^{-1}
10^0
10^1
10^{-1}
10^0
10^1
frequency, Hz
frequency, Hz

Figure 12

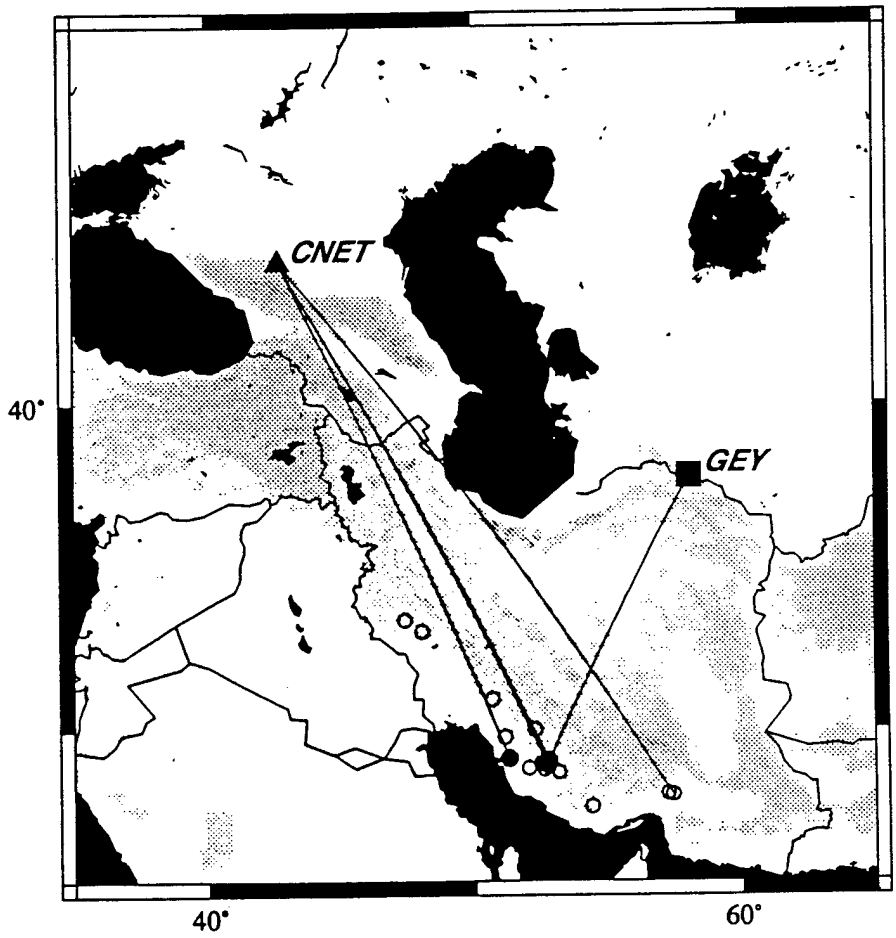

Figure 13

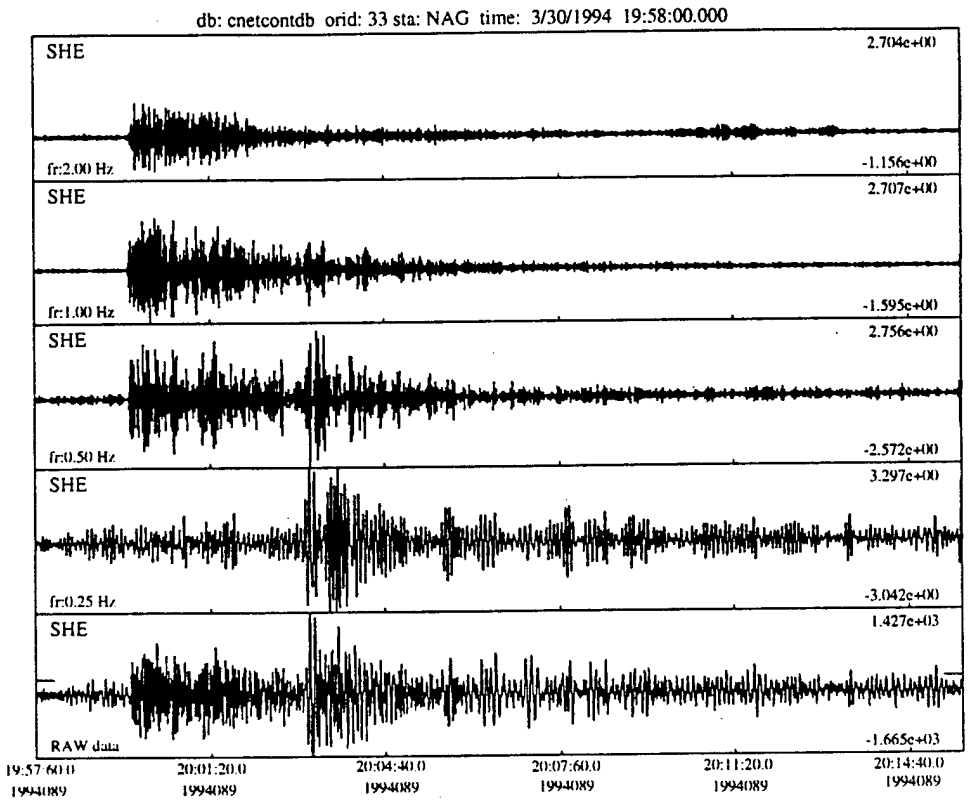
db: cnetcontdb orid: 33 sta: NAG time: 3/30/1994 19:58:00.000
SHE
2.704e+00
fr:2.00 Hz
-1.156e+00
SHE
2.707e+00
fr:1.00 Hz
-1.595e+00
SHE
2.756e+00
fr:0.50 Hz
-2.572e+00
SHE
3.297e+00
fr:0.25 Hz
-3.042e+00
SHE
1.427e+03
RAW data
-1.665e+03
19:57:60.0
1994089
20:01:20.0
1994089
20:04:40.0
1994089
20:07:60.0
1994089
20:11:20.0
1994089
20:14:40.0
1994089

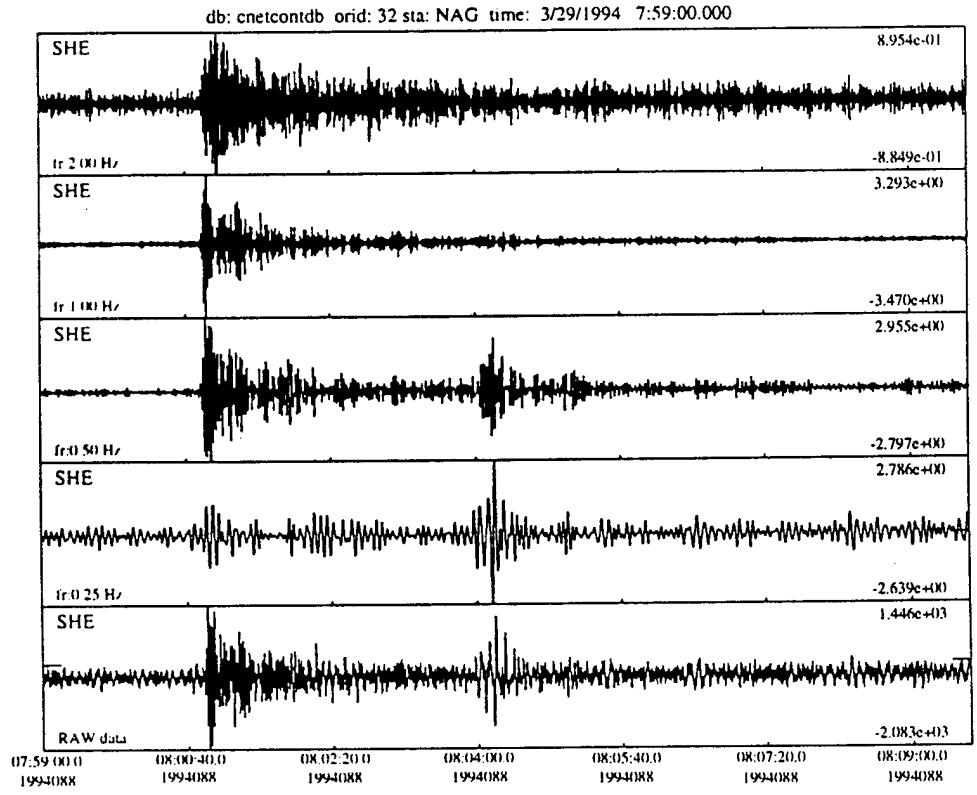
db: cnetcontdb orid: 32 sta: NAG time: 3/29/1994 7:59:00.000
SHE
8.954e-01
fr 2.00 Hz
-8.849e-01
SHE
3.293e+00
fr 1.00 Hz
-3.470e+00
SHE
2.955e+00
fr:0.50 Hz
-2.797e+00
SHE
2.786e+00
fr:0.25 Hz
-2.639e+00
SHE
1.446e+03
RAW data
-2.083e+03
07:59:00.0
1994088
08:00:40.0
1994088
08:02:20.0
1994088
08:04:00.0
1994088
08:05:40.0
1994088
08:07:20.0
1994088
08:09:00.0
1994088

Figure 14

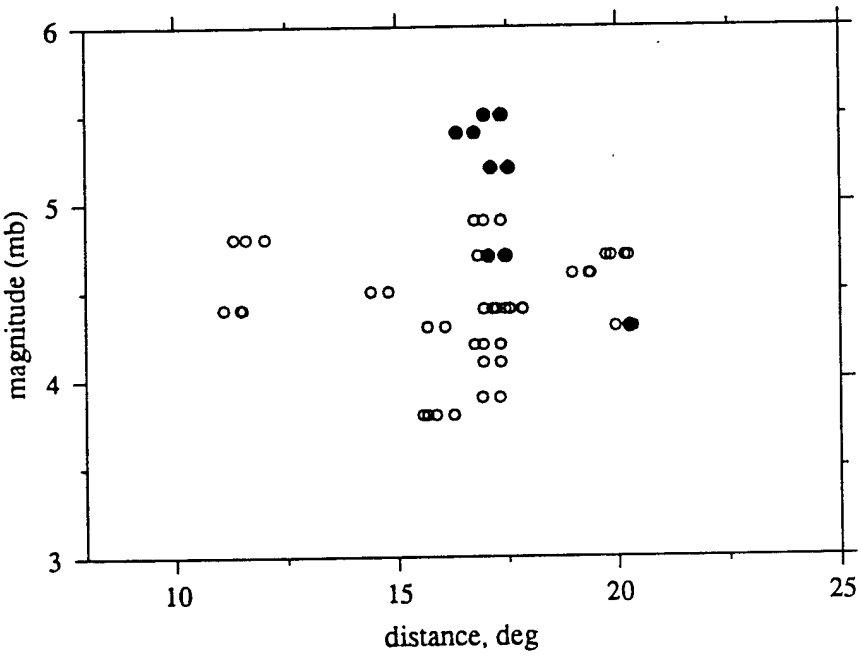

Figure 15

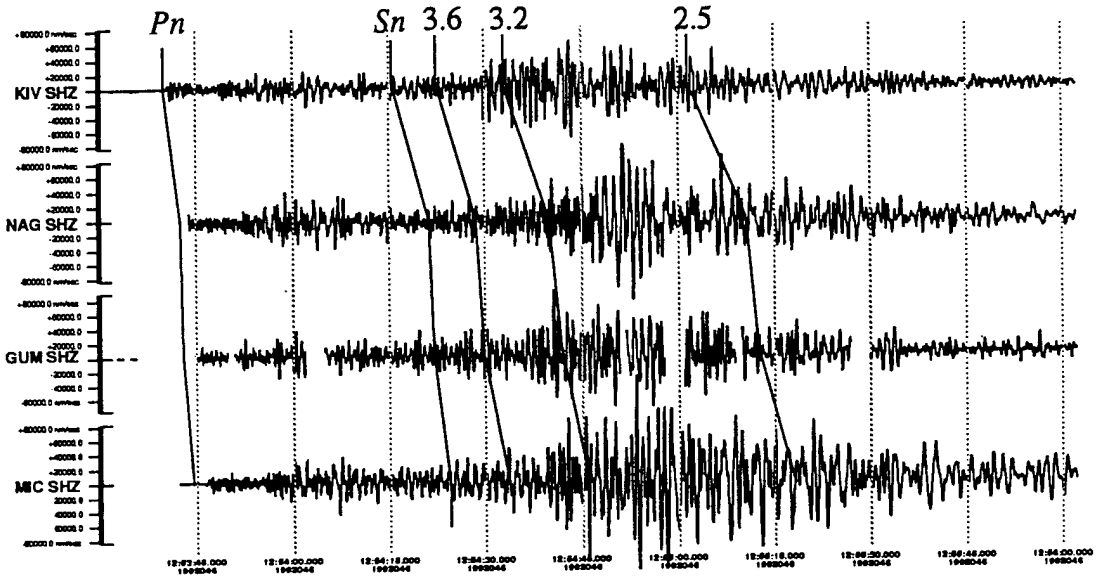

Event 020 Delta 2.91-3.30 seaz 110-125 mb4.9

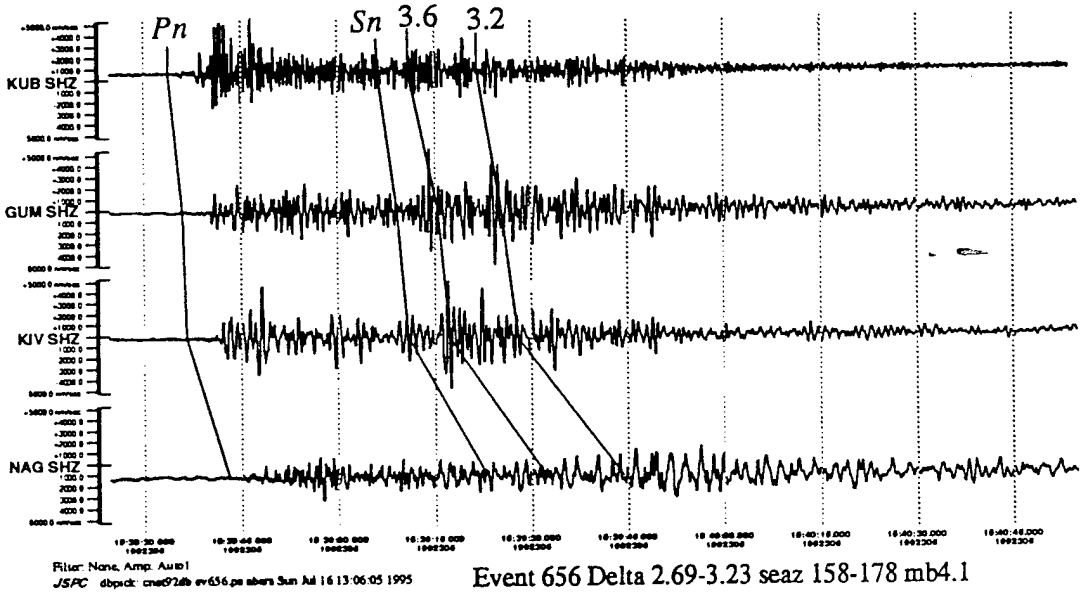

Event 656 Delta 2.69-3.23 seaz 158-178 mb4.1

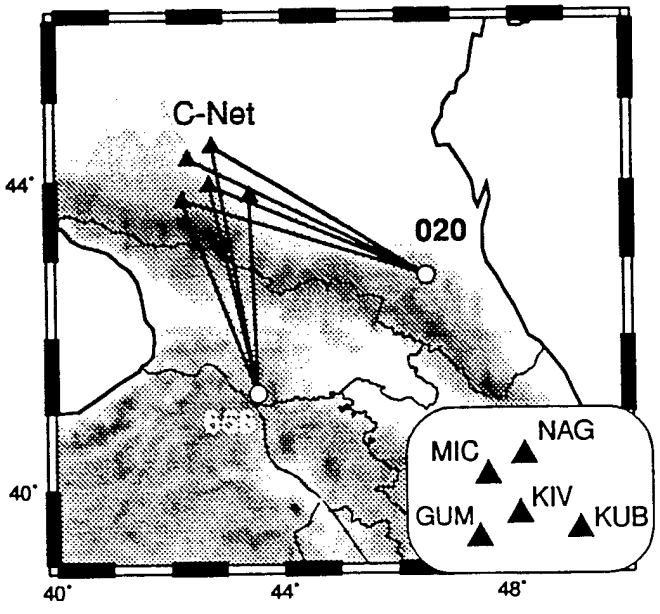

Figure 16

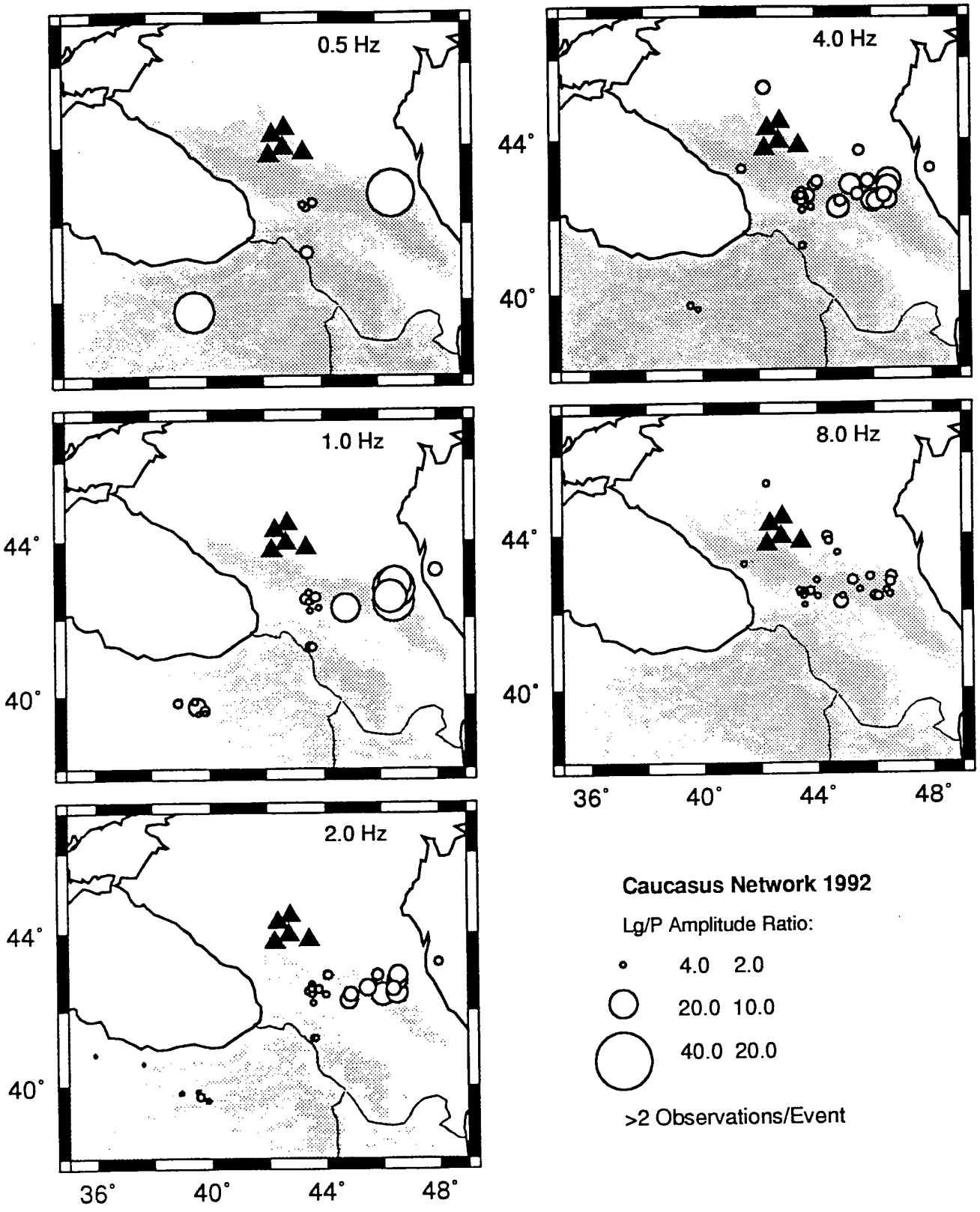
0.5 Hz
4.0 Hz
1.0 Hz
8.0 Hz
2.0 Hz
44°
40°
36°
40°
44°
48°
Caucasus Network 1992
Lg/P Amplitude Ratio:
4.0 2.0
20.0 10.0
40.0 20.0
>2 Observations/Event

Figure 17.

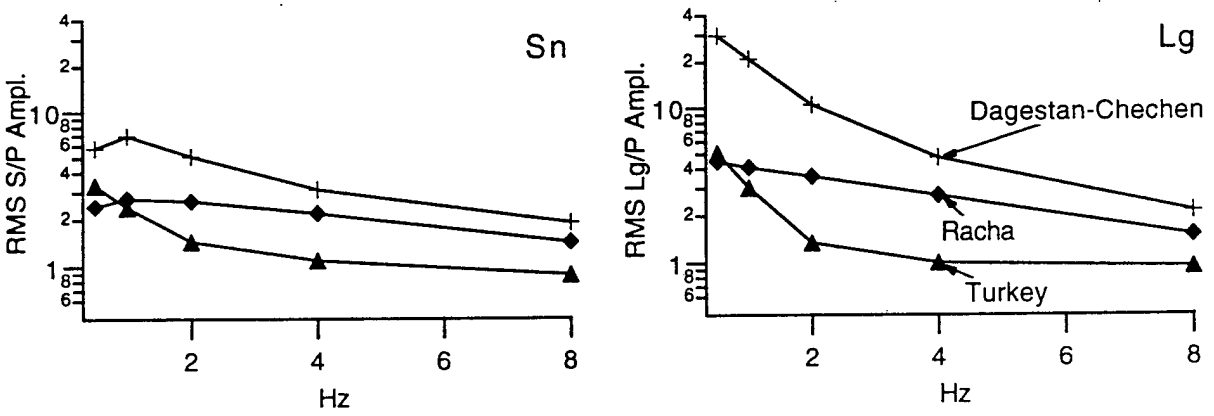
Sn
RMS S/P Ampl.
Hz
Lg
RMS Lg/P Ampl.
Dagestan-Chechen
Racha
Turkey
Hz

Figure 18

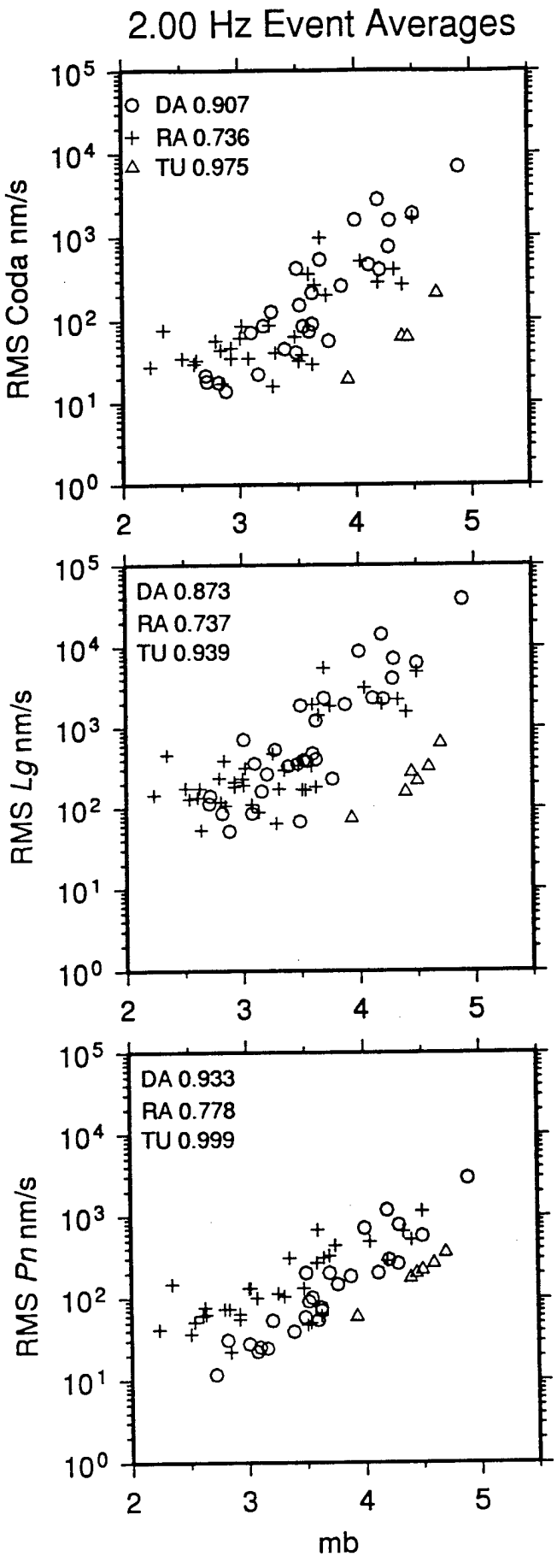
2.00 Hz Event Averages
RMS Coda nm/s
DA 0.907
RA 0.736
TU 0.975
RMS Lg nm/s
DA 0.873
RA 0.737
TU 0.939
RMS Pn nm/s
DA 0.933
RA 0.778
TU 0.999
mb

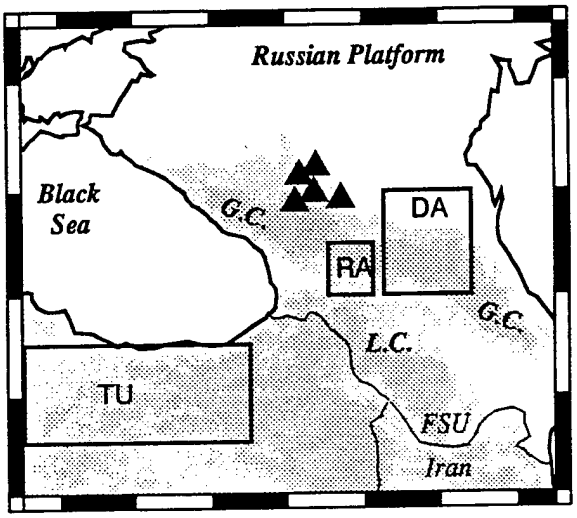
Russian Platform
Black Sea
G.C.
DA
RA
G.C.
L.C.
TU
FSU
Iran

Table 1 : t*(r) fitting parameters for each station and network average

station	P wave				S wave			
	mountain path		platform path		mountain path		platform path	
	1000/Q	t*(0)	1000/Q	t*(0)	1000/Q	t*(0)	1000/Q	t*(0)
KIV	1.13 ± 0.30	.0163 ± .0075	0.19 ± 0.25	.0225 ± .0076	1.25 ± 0.21	.0087 ± .0080	0.32 ± 0.1	.0270 ± .0053
GUM	0.97 ± 0.29	.0310 ± .0072	0.81 ± 0.22	.0240 ± .0070	1.01 ± 0.40	.0284 ± .0160	0.44 ± 0.16	.0155 ± .0072
NAG	0.40 ± 0.60	.0373 ± .0200	0.63 ± 0.24	.0204 ± .0070	1.62 ± 0.37	.0299 ± .0210	0.58 ± 0.14	.0266 ± .0090
MIC	0.42 ± 0.65	.0458 ± .0211	0.15 ± 0.12	.0254 ± .0048	1.06 ± 0.35	.0396 ± .0110	0.30 ± 0.09	.0514 ± .0076
KUB	1.98 ± 0.49	.0121 ± .0119	1.19 ± 2.89	.0137 ± .0076	1.24 ± 0.37	.0359 ± .0138	0.53 ± 0.24	.0467 ± .0100
All[1]	0.93 ± 0.17 Q = 1070 ± 200	.0257 ± .0046	0.47 ± 0.12 Q = 2130 ± 600	.0221 ± .0038	1.29 ± 0.12 Q = 775 ± 75	.0194 ± .0057	0.49 ± 0.07 Q = 2060 ± 315	.0263 ± .0039
All[2]	0.93 ± 0.27 Q = 1076 ± 353	.0325 ± .0080	0.45 ± 0.20 Q = 2225 ± 687	.0037 ± .0071	1.40 ± 0.14 Q = 708 ± 70	.0225 ± .0062	0.55 ± 0.11 Q = 1860 ± 385	.0349 ± .0073

1 : unconstrained corner frequency
2 : constrained corner frequency

Table 2 : Description of inversion parameterization

Model Type	Description	# free parameters	Variances, $x10^{-3}$ s^2 P–wave	S–wave
A	homogeneous half–space	1	0.705	1.543
B	2 layer, 1 block in each layer	2	0.541	1.474
C	1 layer and 2 blocks	2	0.578	1.115
D	2 layer, 2 blocks in each layer	4	0.463	1.091
E	2 layer, 1 block/station in top homogeneous lower layer	7	0.464	0.971
F	2 layer, 1 block/station in top 2 blocks in lower layer	8	0.380	0.637
G	3 layer, 1 block/station in top 2 crustal blocks 1 mantle block	9	0.381	0.675
H	3 layer, 1 block/station in top lower layers similar to F	10	0.375	0.635
I	2 layer, 1 block/station in top lower layer thin blocks	17	0.369	0.638
J	3 layer, 1 block/station in top lower layers similar to I	28	0.341	0.609
K	2 layer, 1 block/station in top 80 km x 80 km block lower	48	0.341	0.618

	Table 3 : Events from S. Iran found in Caucasus and Geyokcha triggered catalog										
orid	latitude	longitude	origin.time	depth	delta	SEAZ	mb	nass	signals seen?	compared to triggered NET	sta list in triggered catalog
21	30.0070	52.2480	10/13/1993 (286) 0:11:04.700	33.0000	15.880	148.27	3.80	12	no	Caucasus	
22	29.7730	51.1030	10/23/1993 (296) 13:26:42.100	33.0000	15.683	151.95	4.30	8	no	Caucasus	
23	27.8880	57.4150	11/01/1993 (305) 6:42:00.800	33.0000	19.947	138.79	4.30	8	KIV @ 1 hz	Caucasus	NAG
24	28.7590	51.9900	11/03/1993 (307) 16:42:17.600	33.0000	16.920	150.85	3.90	6	no	Caucasus	
25	27.9200	57.2340	3/03/1994 (062) 14:56:48.900	33.0000	19.835	139.14	4.70	10	no	Caucasus	
26	28.9000	52.4650	3/03/1994 (062) 23:54:01.000	33.0000	16.962	149.35	4.90	10	GUM KIV MIC NAG KNG @ 2 Hz	Caucasus	no records bet 2/14/94 & 3/25/94 in catalog
27	29.0260	52.7260	3/07/1994 (066) 0:57:19.600	10.0000	16.945	148.45	4.20	10	no	Caucasus	
28	33.1460	48.0330	3/07/1994 (066) 10:54:57.400	26.0000	11.587	157.13	4.80	8	no	Caucasus	
29	28.6330	53.1290	3/19/1994 (078) 4:54:00.300	33.0000	17.452	147.95	4.40	10	no	Caucasus	
30	28 7270	52.5880	3/19/1994 (078) 5:57:04.600	33.0000	17.164	149.26	4.40	10	no	Caucasus	
31	28 8740	52.5960	3/23/1994 (082) 17:14:45.300	33.0000	17.034	149.03	4.70	10	no	Caucasus	
32	29 0960	51.2560	3/29/1994 (088) 7:56:53.900	33.0000	16.359	152.45	5.40	8	yes @ 2 Hz	Caucasus	GUM KIV NAG MIC
33	28 9940	52.7450	3/30/1994 (089) 19:55:46.000	54.0000	16.981	148.45	5.50	8	yes @ 2 Hz	Caucasus	GUM KIV NAG MIC
33	28 9940	52 7450	3/30/1994 (089) 19:55:46.000	54.0000	7 38	227.20	5.50	-	yes @ 2 Hz	Geyokcha	A-H series ORGH ORGL SEL SWH SWL
34	28 8210	52 7450	4/03/1994 (093) 8:51:57.500	23.0000	17 137	148 70	5.20	8	yes @ 2 Hz	Caucasus	NAG GUM KIV
35	28 8870	52 7050	4/03/1994 (093) 7:19:36 300	33.0000	17 062	148 71	4.70	8	yes @ 2 Hz	Caucasus	NAG GUM KIV
36	27 4770	54 3850	4/21/1994 (111) 11:50:32.600	33 0000	18 979	146 41	4.60	8	no	Caucasus	
37	30 9990	50 6350	4/26/1994 (116) 6:26:01 800	33.0000	14 397	151.52	4.50	8	no	Caucasus	
38	29 0080	52 6870	4/30/1994 (120) 23:11:13.400	33 0000	16 946	148.59	4.10	8	no	Caucasus	
39	33 5010	47 3840	5/03/1994 (123) 20:20:18 800	33 0000	11 077	159.16	4.40	8	no	Caucasus	